Remaining aerosol forcing uncertainty after observational constraint and the processes that cause it

Leighton A. Regayre[1,2,3], Léa M. C. Prévost[3], Kunal Ghosh[3], Jill S. Johnson[4], Jeremy E. Oakley[4], Jonathan Owen[3,4], Iain Webb[4] and Ken S. Carslaw[3]

[1]Met Office Hadley Centre, Exeter, Fitzroy Road, Exeter, Devon, EX1 3PB, UK
[2]Centre for Environmental Modelling and Computation, University of Leeds, Leeds, LS2 9JT, UK
[3]School of Earth and Environment, School of Earth and Environment, University of Leeds, Leeds, LS2 9JT, UK
[4]School of Mathematical and Physical Sciences, University of Sheffield, Sheffield, S3 7RH, UK

Correspondence to: Leighton A. Regayre (Leighton.Regayre@metoffice.gov.uk)

Abstract. Aerosol radiative forcing remains a major source of climate model uncertainty, limiting climate model projection skill and slowing global action on addressing climate risks. Observations only modestly constrain the magnitude of aerosol radiative forcing despite advances in model fidelity, resolution and availability of observations. Our goals are to understand where aerosol-cloud forcing uncertainty resists efforts to reduce (or constrain) it and to identify the processes that cause the remaining uncertainty, to guide future observation campaigns and model constraint efforts. We map the aerosol forcing uncertainty in a global climate model perturbed parameter ensemble before and after constraint to satellite observations of several cloud, aerosol and radiative properties. Original uncertainty falls by more than 80 % in Northern Hemisphere marine regions and by 70 % for globally averaged aerosol forcing. However, the uncertainty remains large (more than 70 % of the original uncertainty) in Southern Hemisphere marine environments where stratocumulus clouds transition to cumulus, as well as in some highly populated industrialized areas. Regional clusters of shared causes of model uncertainty highlight common processes as targets for future observational constraint. Our findings highlight the value in re-evaluating the remaining causes of ΔF_{aci} uncertainty during the constraint process and provide actionable information for prioritizing existing observations that should be included as constraints. Additionally, our results highlight targeted observations in persistent uncertainty hotspots where novel and process-specific data could further constrain aerosol forcing. This work provides a framework for model evaluation and development that prioritises aerosol forcing constraint to improve model skill at making climate projections.

1 Introduction

Aerosol effective radiative forcing (ΔF_{aer}) is one of the largest causes of uncertainty in anthropogenic climate change over the past century (Forster et al., 2021). Whilst the cooling effect of anthropogenic aerosol substantially offsets the warming effect of greenhouse gases, the magnitude of ΔF_{aer} over historical periods is uncertain. Despite decades of improvements to model fidelity, increasing model resolution, and a huge increase in observational data availability, large ΔF_{aer} uncertainty persists (Forster et al., 2021). Model processes that cause uncertainty in historical ΔF_{aer} also cause uncertainty in future climate change (Gettelman et al., 2024), suggesting that narrowing the model process uncertainty in ΔF_{aer} over the historical period could significantly improve confidence in climate projections. Uncertainty in model processes accounts for more than 50 % of the uncertainty caused by highly uncertain future shared socioeconomic pathways (Peace et al., 2020), which translates to around 0.5° C additional uncertainty in long-term warming projections from anthropogenic CO_2 emissions (Watson-Parris and Smith, 2022). Reduction in ΔF_{aer} uncertainty would also help to understand aerosol influence on clouds and atmospheric circulation patterns (Mülmenstädt and Wilcox, 2021; Peace et al., 2022), and to reduce some of the risks associated with mitigating the impacts of future climate change.

Climate models are imperfect partly because they represent physical processes using parametrizations – mathematical approximations to real-world processes that are designed to balance fidelity with computational efficiency. Differences in the magnitude of ΔF_{aer} across climate models stem from choices about how to parameterize physical processes (Bellouin et al., 2020). The approximate nature of these parametrizations introduces inherent discrepancies between models and observations that cannot be overcome through parameter retuning (Sexton et al., 2012). For aerosol-cloud interactions, governing processes are microphysical, so the fundamental mismatch in scale with global climate simulations ensures model-observation discrepancies will likely persist even in simulations where resolution is increased to feasible computational limits (e.g. Hoffmann et al., 2023). As a result, no climate model can be fully constrained by observations and will always be partly limited

by observational error, spatial and temporal representation errors (Schutgens et al., 2017), and inherent model biases (e.g. Liu et al., 2024; Price et al., 2025).

Closer collaboration between climate modelers, lab-based experimentalists, in-situ observation teams, and satellite instrument scientists has been viewed as essential for improving our ability to constrain ΔF_{aer} (Kahn et al., 2023). However, despite observational programs sharing common goals with modelers to either reduce ΔF_{aer} uncertainty or improve process understanding, modeling centres have yet to provide clear guidance on how new observations can be effectively integrated to reduce model uncertainty, or how priorities for future observational campaigns might evolve in response to better use of existing data.

Meaningful progress with understanding the causes of model uncertainty can be achieved by evaluating (against observations) a wide range of model "variants" that comprehensively sample important causes of uncertainty in ΔF_{aer} (Johnson et al., 2020; Mikkelsen et al., 2024; Regayre et al., 2020, 2023; Rostron et al., 2020; Zhong et al., 2023). These variants can be generated from perturbed parameter ensembles (PPEs) that systematically vary multiple uncertain model parameters to explore the breadth of model behaviour (e.g., Carslaw et al., 2013; Eidhammer et al., 2024; Elsaesser et al., 2025; Qian et al., 2018; Yoshioka et al., 2019). PPE studies, coupled with statistical analyses, have identified key causes of climate model ΔF_{aer} uncertainty. For instance, natural aerosols contribute more to ΔF_{aer} uncertainty over the industrial period than other aerosol sources because of their disproportionate influence on baseline aerosol concentrations (Carslaw et al., 2013), while atmospheric process parameters account for nearly half of the ΔF_{aer} uncertainty through their effect on cloud properties (Regayre et al., 2018).

Narrowing of the uncertainty in ΔF_{aer} (or "constraint") remains a challenge, in part because the causes of ΔF_{aer} uncertainty vary spatially and temporally due to differences in atmospheric conditions and variations in aerosol emissions, dominant processes and evolving climate impacts of aerosol as they age (Regayre et al., 2014). For example, Regayre et al., (2018) showed uncertainty in the radiative properties of black carbon aerosol cause less than 5 % of the global mean ΔF_{aer} uncertainty in most

months but accounts for around 50 % of the annual mean ΔF_{aer} uncertainty near high-emission sources, where black carbon influences boundary layer stability, cloudiness and the susceptibility of clouds to

85   aerosol changes (Bond et al., 2013). Parameters may be overlooked not only when their effects are regionally isolated but also when causes of regional ΔF_{aer} uncertainty cancel out in global mean calculations due to opposing forcing sensitivities across different regions (Regayre et al., 2015). For example, an increase in uncertain natural aerosol emissions can suppress ΔF_{aer} (make it less negative) in relatively clean regions (Carslaw et al., 2013) whilst enhancing ΔF_{aer} (more negative) in polluted

90   regions, where natural and anthropogenic sources combine to increase cloud lifetime (Albrecht, 1989; Regayre et al., 2015). Overcoming these challenges requires leveraging combinations of observations that target specific processes (e.g. Sprintall et al., 2020), or collectively account for uncertainties in aerosol emissions, deposition, size, and composition, as well as microphysical interactions between aerosol and clouds.

95   Observational constraints on ΔF_{aer} uncertainty are limited by three interlinked issues. First, only observations that share causes of uncertainty with ΔF_{aer} can provide meaningful constraint. Second, compensating model errors allow multiple equally-plausible model variants (or equifinal variants; Beven and Freer, 2001) to agree with observations without any narrowing of the credible ΔF_{aer} range. Third, structurally imperfect models are susceptible to contrasting constraints, where two or more

100   observations constrain a model towards non-overlapping sets of parameter combinations. When combined, these contrasting constraints force a compromise in model skill at simulating associated variables, leaving us with models that on average only perform tolerably (Regayre et al., 2023).

These three issues must be considered collectively to identify useful ΔF_{aer} constraints. For example, concentrations of cloud condensation nuclei directly affect the magnitude of ΔF_{aer} and so

105   share causes of uncertainty, but associated observations only weakly constrain ΔF_{aer} because of compensating errors in model microphysics (Lee et al., 2016). Similarly, top-of-the-atmosphere radiative flux measurements suffer from equifinality related to aerosol emission, processing and deposition process uncertainties, so only weakly constrain ΔF_{aer} despite being a key quantity used to calculate ΔF_{aer} (Regayre et al., 2018). Multi-season, multi-location observational data constraints may

partially overcome the equifinality issue by introducing some orthogonality into the overall constraint. However, large observational datasets typically contain a high degree of complementary information, as many observable variables share causes of uncertainty and are therefore somewhat redundant (Regayre et al., 2023). A broad set of observations can actually limit the constraint effectiveness (e.g. Johnson et al., 2020) because using large data sets increases the likelihood of exposing structural model deficiencies (Regayre et al., 2023).

Observations specifically designed (or collated) to isolate differences between present-day and early-industrial environments - such as hemispheric difference in cloud droplet concentrations - more directly map onto ΔF_{aer} (share causes of uncertainty). These observations can bypass much of the error compensation issue by leveraging the large, well-characterized contrast between polluted and pristine environments, so do partially constrain ΔF_{aer} (McCoy et al., 2020). Similarly, aerosol observations from targeted campaigns in pristine environments (e.g. the Antarctic Circumnavigation Expedition – Study of Preindustrial-like Aerosol Climate Effects; ACE-SPACE; Schmale et al., 2019) largely avoid the effects of compensating errors and can uniquely constrain natural aerosol concentrations and their precursors (Regayre et al., 2020), which are critical for reducing ΔF_{aer} uncertainty (Carslaw et al., 2013). However, constraining a model to match a single observation type or environment risks overfitting – yielding a good match for one variable or set of conditions, but with no guarantee of increasing climate projection skill.

To overcome all three limitations, models need to be constrained against a suite of observations that 1) share ΔF_{aer}'s causes of uncertainty, 2) collectively minimize the effect of compensating errors, and 3) expose and avoid the effects of structural model errors. Crucially, the dominant sources of ΔF_{aer} uncertainty will likely shift once any observational constraint is applied. This means the criteria for a "good" constraint may evolve as observational constraints are applied, to better align with changing causes of uncertainty and to address any newly revealed compensating errors or model structural deficiencies.

135   This paper builds on the work of Regayre et al., (2023; hereafter referred to as "R23") to address the challenges outlined above. R23 constrained global, annual mean aerosol-cloud interaction forcing (ΔF_{aci}; the larger component of ΔF_{aer}) in version 1 of the UK Earth System Model (UKESM1; Sellar et al., 2019) by nearly 70 % (reduction in 90 % credible interval width). This "optimal" constraint reduced ΔF_{aci} uncertainty to the maximum limit with their chosen observations and structurally imperfect model.

140 Yet over 30 % of the ΔF_{aci} uncertainty remains, with observationally plausible ΔF_{aci} values ranging from -0.9 to -0.1 W m^{-2} (90 % credible interval) and regional uncertainties up to around 20 W m^{-2}.

     To further constrain ΔF_{aci} towards the limits imposed by observational uncertainties, several key challenges must be addressed. First, we must distinguish between regions where ΔF_{aci} uncertainty has been constrained and regions where the chosen observations had a weaker effect. Second, we need to

145 identify the model parameters that cause remaining ΔF_{aci} uncertainty and how their contributions vary regionally. Third, we must determine which existing or future observations would best constrain these remaining causes of ΔF_{aci} uncertainty. Tackling these challenges would optimize the use of available observations and guide future campaigns, creating a feedback cycle between model evaluation and refinement, and observational design, as exemplified by Carslaw et al., (2013), Hamilton et al., (2014),

150 Schmale et al., (2019) and Regayre et al., (2020).

     Section 3.1 examines how each observation added to the R23 optimal constraint reduces ΔF_{aci} uncertainty by eliminating specific parameter combinations. **Section 3.2** maps the remaining uncertainty, revealing significant heterogeneity in constraint efficacy. **Section 3.3** identifies the causes of remaining regional and global mean ΔF_{aci} uncertainty, and **Section 3.4** clusters regions according to

155 shared causes of uncertainty and identifies priorities for model development and future observation campaigns. Finally, **Section 4** discusses the potential for further ΔF_{aer} constraint across the current generation of climate models, and ways the scientific community might collaborate to achieve this elusive goal.

2 Methods

160 Regayre et al., (2023) used version 1 of the UK Earth System Model (UKESM1; Sellar et al., 2019) to create a 221-member PPE that spans model responses to changes in 37 uncertain aerosol, cloud, and physical atmosphere model parameters (Appendix A Table A1). Statistical emulators of multiple variables were used to scale up from 221 ensemble members to 1 million model variants (parameter combinations) which is sufficiently large to allow for robust observational constraint using more than 450

165 observations (Section 2.3), to identify localized model behaviour linked to specific parameters (Section 2.4) and variance-based sensitivity analyses (Section 2.5).

Regayre et al., (2023) identified the observation type that provided the strongest ΔF_{aci} constraint, then progressively added the next strongest observation, eventually reducing ΔF_{aci} uncertainty by nearly

170 70 % using a combination of just 13 observation values. In this study, we build on the R23 foundation by analyzing the causes of the remaining 30 % of ΔF_{aci} uncertainty after optimal constraint. We quantify parameter contributions to remaining ΔF_{aci} uncertainty at the model grid box level and within clusters of shared causes of uncertainty (Section 2.5).

175 ## 2.1 Experimental design

Regayre et al. (2023) used the atmosphere-only configuration of UKESM1 to create their PPE. UKESM1 is based on the HADGEM3-GC3.1 physical climate model (Williams et al., 2018) with additional coupling to key Earth system processes, including the United Kingdom Chemistry and Aerosol (UKCA) model (Archibald et al., 2020). The atmosphere-only configuration (UKESM1-A)

180 consists of the GA7.1 atmosphere (Walters et al., 2019), with additional aerosol, cloud, and physical atmosphere structural updates as implemented in Mulcahy et al., (2020). R23 used UKESM1-A at N96 horizontal resolution, which is 1.875° ×1.25° (208 km×139 km at the Equator), with 85 vertical levels unevenly distributed between the surface and 85 km in altitude, matching the model version submitted to the 6th Coupled Model Intercomparison Project (CMIP6; Eyring et al., 2016). They nudged

185 horizontal wind fields above around 2 km (model vertical level 17) towards ERA-Interim values for the

7

period December 2016 to November 2017 and prescribed sea ice and sea surface temperatures for the same period.

190 The model PPE members were forced using anthropogenic SO_2 emissions for the years 2014 and 1850, as prescribed in CMIP6 simulations. Differences in top-of-the-atmosphere radiative fluxes between the two anthropogenic emission periods were used to calculate ΔF_{aer} values. The components of ΔF_{aer} from aerosol-cloud interactions, ΔF_{aci}, and aerosol-radiation interactions (ΔF_{ari}) account for above-cloud aerosol radiative effects (Ghan et al., 2016) and multiple cloud adjustments (Forster et al., 2021; Grosvenor and Carslaw, 2020). Carbonaceous aerosol emissions were prescribed using CMIP6
195 (1850) and Copernicus Atmospheric Monitoring Service (CAMS; 2016-17) data, whilst ocean surface concentrations of dimethylsulfide (DMS) and chlorophyll, as well as atmospheric concentrations of gas species (including oxidants OH and O_3) were prescribed using monthly mean output from a fully coupled version of the UKESM model averaged over the 1979 to 2014 period. Additionally, R23 prescribed volcanic SO_2 emissions for continuously emitting and sporadically erupting volcanoes
200 (Andres and Kasgnoc, 1998) and for explosive volcanic eruptions (Halmer et al., 2002).

Regayre et al. (2023) made structural changes to UKESM1-A to better sample the breadth of ΔF_{aci} uncertainty. Following Yoshioka et al., (2019), an ice mass fraction threshold was defined, above which no nucleation scavenging occurs, to allow sufficient aerosol to be transported to the Arctic
205 (Browse et al., 2012). They also included an organically mediated aerosol nucleation parameterisation (Metzger et al., 2010) to represent remote marine and early industrial aerosol concentrations more accurately in the model. Additionally, R23 used high-resolution lookup tables for aerosol optical properties (Bellouin et al., 2013) that include properties for mineral dust (Balkanski et al., 2007) and better resolve aerosol absorption.

210 **2.2 Perturbed parameter ensembles and emulation**

The Regayre et al. (2023) PPE was created in two stages using a history-matching style approach (Craig et al., 1997; Williamson et al., 2013) to ensure that the 221 ensemble members (parameter

combinations) spanned the 37-dimensional parameter space whilst achieving acceptable agreement with large-scale climate metrics. Following Lee et al., (2012), Regayre et al., (2014), Sexton et al., (2021) and Yoshioka et al., (2019), ranges for the 37 uncertain parameters were determined by formal expert elicitation using the Sheffield Elicitation Framework (SHELF) approach described in Gosling (2018).

215

Statistical Gaussian Process emulators (O'Hagan, 2006) were used to extend the 221 climate model simulations to 1 million model variants. Emulators can very efficiently predict output for new model variants (parameter combinations) compared to the time and computational resource required to create climate model ensemble members. Furthermore, as opposed to other machine-learning approaches, emulator uncertainty can be quantified for any parameter combination, to validate emulator skill and avoid over-constraint when comparing model variant output to observations (e.g. Johnson et al., 2020).

220

225

Regayre et al. (2023) created statistical emulators of a) global mean ΔF_{aer} and its components ΔF_{aci} and ΔF_{ari}, b) regional mean cloud and radiative properties, and c) values from transects spanning stratocumulus- to cumulus-dominated regions (Section 2.3). In total, they created and evaluated around 450 statistical emulators. Here, we create emulators of annual mean ΔF_{aci} at the model grid box level. Thus, we densely sample model ΔF_{aci} uncertainty, at more than 27 000 geographical locations, using the same set of 1 million model variants (parameter combinations).

230

2.3 Observational constraint

Regayre et al. (2023) constrained ΔF_{aci} using multiple satellite-derived cloud and radiation properties. Observations used for constraint included liquid water path (LWP), liquid cloud fraction (f_c), cloud optical depth (τ_c), and cloud droplet effective radius (r_e) from the MODIS instruments (King et al., 2003). τ_c and r_e values were used to calculate cloud droplet number concentration (N_d) values. Observational constraints also included outgoing top-of-the-atmosphere shortwave radiative flux (F_{SW}) measurements from the Clouds and the Earth's Radiant Energy System experiment (CERES; Loeb et al., 2018). Regional mean

235

240   observations were derived for regions of persistent stratocumulus cloud in the North and South Atlantic,

North, and South Pacific and Southern Ocean. R23 also used hemispheric differences in marine N_d for

constraint (H_d), as well as multiple relationships between aerosol, cloud, and radiation properties along

transects from stratocumulus- to cumulus-dominated regions.

245   In total, R23 evaluated the ΔF_{aci} constraint potential of more than 450 observations (more than 66

variables in 5 regions at multiple times). Nearly half of these observations were removed from the R23

constraint method because they were identified as being associated with model structural deficiencies,

revealed through pair-wise analysis of constraints using the original 1 million model variants. Structural

model deficiencies lead to inconsistencies in pairs of model variables, where they constrain the model

250   towards non-overlapping sets of parameter combinations (referred to as the history-matching "terminal

case"; Salter et al., 2019). Thus, constraint to one observable variable greatly decreases model skill at

simulating the other, and constraint using both variables forces a compromise towards a set of model

variants with low skill at simulating either. R23 removed variables associated with structural deficiencies

and used the remaining around 250 observations they considered pairwise consistent with N_d, to search

255   of an optimal constraint on ΔF_{aci}.

      The optimal constraint on ΔF_{aci} achieved in R23 made use of just 13 observable variables. The

R23 approach started with the observation that most strongly constrained ΔF_{aci}. They then identified the

most compatible observation that, in combination with the first, provided the strongest constraint on ΔF_{aci}.

260   This process continued by progressively adding the observation that most tightly constrained ΔF_{aci}

uncertainty in combination with the existing set of observations. At each stage of the constraint process,

R23 compared emulator mean and observed values, whilst accounting for statistical emulator uncertainty

to retain a minimum of 5000 model variants and avoid over-constraint. Including additional observable

variables beyond the optimal set weakened the constraint. Hence, R23 described the optimal constraint

265   as the tightest constraint achievable with the chosen set of observations and structurally imperfect model.

2.4 Filtering implausible parameter values

In this article we explore how progressively adding observational constraints in the R23 optimal set affect the plausible ranges of uncertain parameters and the credible range of ΔF_{aci}. We evaluate ΔF_{aci}

270   uncertainty in the "original" set of 1 million model variants and in the "unconstrained" set which excludes implausible parameter values that would otherwise dominate analysis of the effects of observational constraints on other parameters.

For most parameters, the R23 ΔF_{aci} constraint affects the likelihood of some parameter values, as seen in the marginal distributions which are no longer uniform (Fig. S12 and S13 of Regayre et al., 2023).

275   That is, in the set of model variants that agree with observations, a given parameter value is more likely to have a higher or lower value (as per the marginal distribution) than in the release version of the model. However, for the parameters related to cloud droplet activation (cloud updraft speed; *sig_w*) and the diameter of primary sulfate particles (*prim_so4_diam*), the constraint is stronger and ruled out part of the parameter range as observationally implausible - i.e., there is no way of combining these ruled out

280   parameter values with the other 36 model parameters to bring them into agreement with observations (See R23 Figs S12 and S13).

In the original set of 1 million model variants, ΔF_{aci} is only sensitive to *prim_so4_diam* parameter values in a very narrow part of the parameter range (Appendix A Fig. A1). For *prim_so4_diam* values

285   lower than 10 nm, number concentrations are so high that they implausibly suppress cloud formation in the simulated present-day atmosphere, hence these values were ruled out by the R23 constraint. The dominance of implausibly low primary sulfate diameter effects inflated the relative importance of this parameter in the original sensitivity analysis - a known issue with high-dimensional sensitivity analyses (Saltelli et al., 2019). Thus, our analysis of the remaining ΔF_{aci} uncertainty and the path to achieving the

290   optimal constraint, evaluates ΔF_{aci} uncertainty in the original set of 1 million model variants and in the unconstrained set of around 900 000 model variants associated with primary sulfate diameters larger than 10 nm.

2.5 Causes of remaining variance

295 To quantify the sensitivity of ΔF_{aci} to each of the 37 uncertain model parameters (and more generally, the dependence of ΔF_{aci} on parameters), we fit non-linear Generalized Additive Models (GAMs) to the emulated climate model output, implemented using the "pygam" python package (Servén et al., 2018). GAMs are particularly well-suited for analyzing high-dimensional parameter spaces with heterogeneously distributed data, which suits our needs since observational constraints can remove parts

300 of parameter space and even reduce the range of some parameter values (R23; Section 2.4). We quantify the relative importance of parameters as causes of ΔF_{aci} variance (referred to throughout as "causes of uncertainty"), using variance-based sensitivity analyses (Strong et al., 2014). Following R23, we quantify the sum of parameter effects on ΔF_{aci} variance then calculate the proportion of this total that is caused by each parameter. However, the relative importance values here differ from R23 because the GAM method

305 accounts for non-linearities in ΔF_{aci} dependence on changing parameter values, whereas R23 used partial correlations which primarily capture the strength of linear relationships.

Here, marginal variances are calculated by setting all other parameters to the median of the original or constrained sample, then evaluating output from the GAM function. Although the GAM fit is

310 multi-dimensional, this approach allows us to derive ΔF_{aci} variances that are only affected by changes in the target parameter. Using the GAM approach, we can robustly quantify causes of remaining uncertainty after each observational constraint, or combination of constraints, is applied, by calculating marginal sensitivities over the partially reduced parameter space. Thus, this approach can provide insight into how the relative importance of model parameters as causes of ΔF_{aci} uncertainty evolve as observational

315 constraints are progressively added to achieve the R23 optimal set.

2.6 Regional clusters of model behaviour

We use K-means clustering (Pedregosa et al., 2011) to identify distinct sets of model behaviour. K-means clustering is an unsupervised machine-learning technique, that partitions data into clusters of similar behaviour, based on similarity to cluster means. In our case, K-means clusters are defined using

320 proportional contributions to ΔF_{aci} uncertainty from 37 model parameters, across more than 27,000

geographical locations. Using this approach, we identify regions of shared causes of ΔF_{aci} uncertainty in model variants from a) the original set of 1 million, b) the unconstrained set of around 900,000, and c) in the optimally constrained set of 5,000.

3 Results

325 We frame our evaluation of the processes that cause remaining ΔF_{aci} uncertainty in three stages:

1. Evaluate how causes of global mean ΔF_{aci} uncertainty change as each observational constraint was added in R23 (Section 3.1). This approach will be used to isolate the effect of each observation on processes-level uncertainties and to highlight how observational constraints combine to form an overall optimal constraint.

330 2. Quantify causes of remaining ΔF_{aci} uncertainty at the model grid box level (Section 3.2). By doing so, we aim to identify any parameters with spatially coherent influence on remaining ΔF_{aci} uncertainty (Section 3.3).

3. Group the causes of model ΔF_{aci} uncertainty at the grid box level into clusters with similar causes of parametric uncertainty (Section 3.4). We evaluate these spatial patterns to understand where

335 the R23 constraint was strong and where it was weak, and to identify existing and novel observations that could further constrain ΔF_{aci}.

3.1 The effect on the causes of ΔF_{aci} uncertainty of progressively adding observations

Regayre et al. (2023) analyzed one-at-a-time perturbation experiments and evaluated shared causes of
340 uncertainty (between ΔF_{aci} and observable variables) to provide hypotheses about which of the 13 observations in the optimal set most likely contributed to constraining model parameters. Here, we use GAM analyses (Section 2.5) to examine the changes in parametric causes of ΔF_{aci} uncertainty more closely as each constraint is applied.

345 Fig. 1 shows the most important parametric causes of global mean ΔF_{aci} uncertainty for the original set of 1 million model variants and for the uncertainty that remains after progressively applying constraints until the R23 optimal constraint is reached. The parameter controlling the emission diameter

of primary sulfate aerosol (*prim_so4_diam*) is the dominant cause of ΔF_{aci} uncertainty (around 55 % of uncertainty) in the original set of model variants (See section 2.4; Appendix A Table A2). The cloud

350   updraft velocity parameter (*sig_w*), which affects droplet activation, causes around 14 % of the ΔF_{aci} uncertainty and several other parameters related to natural aerosol emission fluxes and removal processes each cause around 5 to 10 % of the ΔF_{aci} uncertainty (Appendix A Table A2). The small number of model parameters affecting the original ΔF_{aci} uncertainty suggests that an informed choice of observations could achieve strong constraint. However, we find that the relative importance of uncertainty sources changes

355   as constraints are progressively applied. Parameters that initially seem unimportant contribute more than a few percent to the remaining uncertainty after constraint, which suggests in-depth analysis may reveal observations with potential to further constrain ΔF_{aci}.
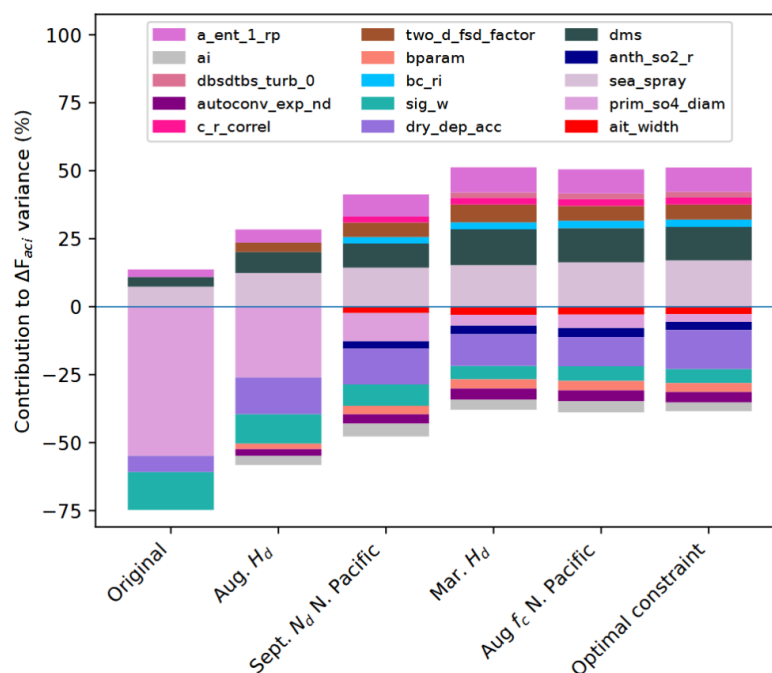

360   Fig. 1. Causes of uncertainty in ΔF_{aci} for the original set of 1 million model variants, and after observational constraint to August H_{d} (Aug. H_{d}), then progressively adding North Pacific N_{d} in September (Sept. N_{d} N. Pacific), March H_{d} (Mar. H_{d}), North Pacific f_{c} in August (Aug. f_{c} N. Pacific) and finally, for the R23 optimal constraint. Only parameters that cause at least 2 % of the uncertainty are shown. See Appendix A Table A2 for contributions from all parameters. Parameter contributions to uncertainty are multiplied by the sign of linear ΔF_{aci} sensitivity to increasing parameter values, thus for parameters below the

365   zero line, increasing the parameter value reduces ΔF_{aci}, making it more negative.

14

The first of the 13 observational constraints used to achieve the R23 optimal constraint is H_d in August. Observed H_d provides a contrast between marine N_d in the polluted Northern Hemisphere (NH) and the relatively pristine Southern Hemisphere (SH), which can act as a proxy for the difference in N_d

370   between the present-day and early-industrial atmospheres (McCoy et al., 2020). Constraint to match observed H_d in August reduces the proportion of uncertainty caused by primary sulfate (*prim_so4_diam*) from around 55 % to only around 25 % and the proportion caused by cloud droplet activation (*sig_w*) from around 14 % to around 11 % (Fig. 1 and Appendix A Table A2). The *sig_w* parameter is constrained towards lower values (R23 SI Fig. S12), consistent with lower N_d concentrations in updraft-limited

375   (mostly polluted NH) regions (Reutter et al., 2009), lower H_d (see R23 SI Fig. S16) and thus weaker (less negative) ΔF_{aci} (Fig. 1; below the zero line indicates increasing the sig_w parameter value strengthens ΔF_{aci}). The *prim_so4_diam* parameter is constrained towards higher values which is also consistent with lower NH N_d and lower H_d values (R23 SI Fig., S16; Cao et al., 2023). However, increasing primary sulfate diameters is associated with stronger (more negative) ΔF_{aci} (Fig. 1) due to the dominant influence

380   of the smallest particle diameter values on the ΔF_{aci} dependence on this parameter (Section 2.4 and SI Fig. 1). Thus, the August H_d observation rules out the strongest and weakest ΔF_{aci} values (tails of the ΔF_{aci} distribution) reducing the 90 % credible range from (-1.6 to 1.0 W m^{-2}) to (-1.2 to 0.2 W m^{-2}). This significant reduction in importance of model parameters that dominate the original uncertainty, using just one observational constraint, highlights the importance of re-evaluating the remaining causes of ΔF_{aci}

385   uncertainty during the constraint process.

Other parameters cause a larger proportion of the remaining ΔF_{aci} uncertainty after August H_d constraint (Fig. 1; Appendix A Table A2). The most prominent increases in importance are in the turbulent cloud top entrainment parameter (*a_ent_1_rp,* a physical atmosphere parameter), natural aerosol emission

390   parameters (*dms* and *sea_salt*) and the aerosol accumulation mode dry deposition velocity (*dry_dep_acc*), for which the contributions to uncertainty approximately double to between 5 % and around 14 %. Several physical atmosphere parameters (*bparam, two_d_fsd_factor, autoconv_exp_nd* and *ai*), which caused less than a few percent of the original ΔF_{aci} uncertainty, emerge as important causes of remaining uncertainty

after the H_d constraint. These results suggest over-reliance on selecting observational constraints based

on original causes of ΔF_{aci} uncertainty can be misleading, as these causes of uncertainty are likely to be

amongst the easiest to constrain. In our case, implausibly low primary sulfate emission diameters and too-

high droplet activation mask the influence of other causes of uncertainty, such as a) those that affect the

early-industrial background aerosol concentration (Carslaw et al., 2013) and b) physical atmosphere

parameters that affect ΔF_{aci} by altering the atmospheric state (Regayre et al., 2018).

400

The relative importance of model parameters as causes of remaining ΔF_{aci} uncertainty continues to

evolve as additional observational constraints are applied, although the first few constraints cause the

largest changes (Fig. 1 and Appendix A Table A2). The *prim_so4_diam* and *sig_w* parameters contribute

less to the remaining ΔF_{aci} uncertainty with each additional constraint, to the point where after optimal

constraint, these parameters together contribute only 8 % of the remaining ΔF_{aci} uncertainty compared

with nearly 70 % in the original set of model variants.

A different set of parameters cause the remaining global mean ΔF_{aci} uncertainty, after optimal

constraint, than those causing ΔF_{aci} uncertainty in the original set of model variants (Fig. 1 and Appendix

A Table A2). Several parameters, mostly natural emission flux and physical atmosphere parameters, are

effectively unconstrained by the optimal set of observations, so their contributions to remaining ΔF_{aci}

uncertainty increase with each new observational constraint. Parameters that affect background aerosol

concentrations together cause nearly half of the remaining ΔF_{aci} uncertainty after optimal constraint

(*sea_salt* 17 %, *dry_dep_acc* 14 % and *dms* 12 %). This suggests there is potential for additional

observational constraint of ΔF_{aci} beyond the R23 optimal constraint using, for example, observations in

remote marine regions (Regayre et al., 2020; Schmale et al., 2019). Additionally, several physical

atmosphere parameters together cause around 32% of the remaining ΔF_{aci} uncertainty (*a_ent_1_rp*: 9 %,

two_d_fsd_factor: 6 %, *autoconv_exp_nd*: 4 %, *bparam* and *ai*: 3 % each, and 1 to 2 % from other

parameters), which highlights the need to identify and use observations that will constrain physical

atmosphere processes that cause ΔF_{aci} uncertainty by altering the cloud properties and thus sensitivity to

aerosol (Mülmenstädt et al., 2024).

3.2 Regional constraint and remaining ΔF_{aci} uncertainty

In this section we explore where the R23 optimal constraint has the strongest and weakest effect on ΔF_{aci}

425 uncertainty. Fig. 2a shows that in the original set of 1 million model variants, ΔF_{aci} uncertainty (90 %

credible interval) is concentrated in regions of persistent stratocumulus cloud as expected, since the

radiative properties of clouds in these regions are highly susceptible to aerosol. However, ΔF_{aci} is also

highly uncertain (90 % credible interval range greater than 5 W m^{-2}) over continental regions near to

anthropogenic emission sources, particularly over central China, and South American coastal regions.

430 Over most ocean regions, even those regions far from persistent stratocumulus cloud, the unconstrained

ΔF_{aci} uncertainty exceeds 2 W m^{-2}.
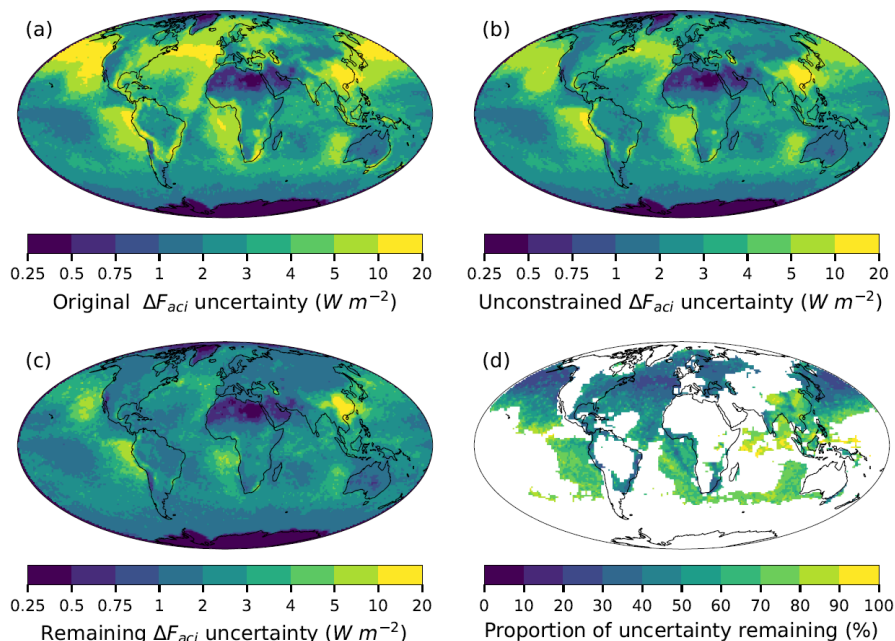
Fig. 2. Annual mean ΔF_{aci} uncertainty (90 % credible interval ranges) in model grid boxes from a) the original set of 1

435 million model variants, b) the unconstrained subset with the lowest prim_so4_diam values filtered out and c) the R23

optimally constrained set of model variants, as well as d) the proportion of original uncertainty remaining after optimal

constraint, in locations where original forcing was greater than 3 W m^{-2}.

Figure 2b shows the effect of removing the 10 % of model variants associated with implausibly low primary sulfate diameters (Section 2.4 and Appendix A Fig. A1). Uncertainty in ΔF_{aci} is reduced to less than 10 W m^{-2} in most regions where it was originally between 10 to 20 W m^{-2} (Fig. 2a). This suggests a significant proportion of ΔF_{aci} uncertainty near anthropogenic emission sources in the original set of model variants was caused by the over-wide perturbed range of the *prim_so4_diam* parameter in R23.

After the optimal constraint, uncertainty in ΔF_{aci} is reduced by between 60 % to 80 % across NH marine regions, most continental regions, in the tropical Atlantic and very prominently along the South-East Atlantic shipping corridor to the west of Africa (Fig. 2 c, d) – note the clear shipping lane in Fig 2d where primary sulfate will have dominated the uncertainty in the original set of model variants. However, there are some regions where ΔF_{aci} uncertainty is largely unaffected by the R23 optimal constraint. For example, over parts of the South Pacific, North-East Pacific and outside the South Atlantic shipping corridor, ΔF_{aci} uncertainty is reduced by less than 30 %, so remains between 4 to 10 W m^{-2}. Additionally, over much of inland China the constraint is less than around 10 % and the remaining uncertainty is more than 10 W m^{-2}. These results suggest there is potential to further constrain ΔF_{aci} using observations that target whichever processes cause remaining uncertainty in these regions.

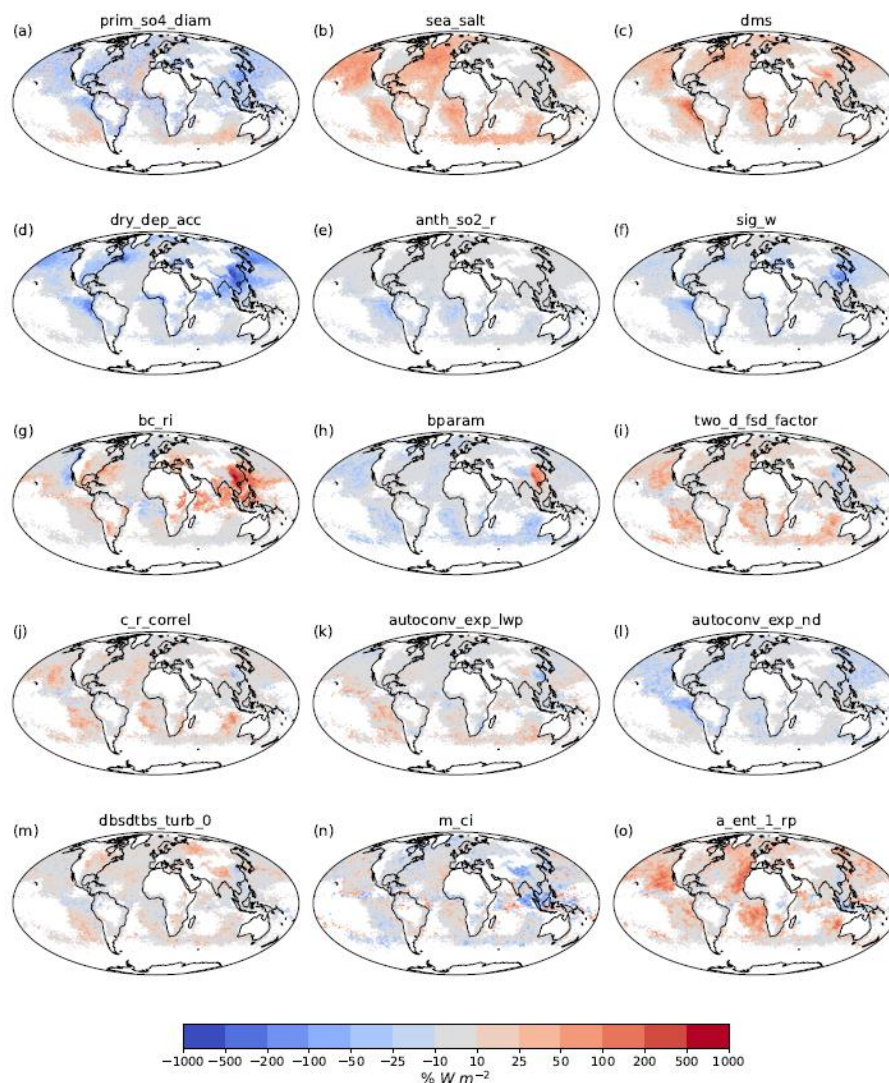## 3.3 Causes of remaining ΔF_{aci} uncertainty at the regional level

In this section we quantify parametric contributions to remaining ΔF_{aci} uncertainty after optimal constraint at the model grid box level. It is essential to constrain sub-global ΔF_{aci} because anthropogenic aerosol can produce regional climate responses that contribute to projection uncertainty (e.g. Chemke and Dagan, 2018; Peace et al., 2022; Shindell, 2014; Williams et al., 2022). Regional variations in the relative importance of parameters as causes of ΔF_{aci} uncertainty can be overlooked by global mean analyses (Regayre et al., 2015). Evaluating uncertainty at the model grid box level can reveal a) cancellation of regional effects in the global mean, where the ΔF_{aci} dependence on model parameters has opposing signs in different regions, b) large but geographically isolated causes of ΔF_{aci} uncertainty that do not stand out in global mean analyses, and c) widespread small contributions to uncertainty that compound to elevate

parameter importance in the global mean analysis. Each of these cases demands a different strategy for further constraint of ΔF_{aci} uncertainty.

470　　Regional patterns of parameter influences on remaining ΔF_{aci} uncertainty reveal a more complex picture than is apparent from an analysis of the global mean (Section 3.1). Figure 3 shows maps of parametric contributions to ΔF_{aci} uncertainty after optimal constraint, weighted by the remaining uncertainty (Fig. 2c) and the sign of ΔF_{aci} dependence on each parameter (as with Fig. 1). These composite maps highlight the parameters that cause remaining uncertainty and the regions where contributions are most pronounced. Although calculations were performed at the model grid box level, Fig. 3 reveals
475 spatially coherent patterns of parameter influences on ΔF_{aci} uncertainty. At the global mean scale, only 6 of the 37 parameters cause 5 % or more of the remaining ΔF_{aci} uncertainty (Fig.1 and Appendix A Table A2) but at the regional scale at least 15 parameters significantly affect ΔF_{aci} uncertainty in multiple regions (Fig. 3) and almost all parameters contribute to remaining ΔF_{aci} uncertainty in at least one region (Appendix A Fig. A2, A3).

480

Fig. 3. Maps of key parametric causes of remaining ΔF_{aci} uncertainty after R23 optimal constraint. Shading indicates the proportion of ΔF_{aci} uncertainty caused by individual parameters, multiplied by the 90 % credible interval range in that grid box and by the sign of the ΔF_{aci} sensitivity to increasing the parameter value. Negative values indicate increasing the parameter value is associated with stronger (more negative) ΔF_{aci} values. Regions where the ΔF_{aci} 90 % CI is less than 3 W m^{-2} are masked.

20

490

The parameters controlling primary sulfate emission diameter (*prim_so4_diam*) and cloud droplet activation (*sig_w*) were tightly constrained by R23 (Fig. 1), but together they still contribute more than 50 % of the remaining ΔF_{aci} uncertainty in some regions, notably over China and the South American 495 coast where more than 50 % of the original uncertainty remains (Fig. 2d). If ΔF_{aci} dependence on these parameters were similar across all regions, the ΔF_{aci} uncertainty would be constrained everywhere. However, the uncertainty caused by these parameters is reduced in some regions but not others, which suggests ΔF_{aci} dependence on *prim_so4_diam* and *sig_w* (in conjunction with other parameter effects) over China and the South Pacific is not the same as the ΔF_{aci} dependence in regions where ΔF_{aci} was more 500 strongly constrained (Fig. 2d).

Several parameters make large-scale, spatially coherent contributions to remaining ΔF_{aci} uncertainty. For example, the *sea_salt* and *dms* parameters are important over most marine environments, contributing 17 % and around 12 % of the remaining global mean ΔF_{aci} uncertainty respectively (Fig. 1). An increase 505 in the magnitude of these natural aerosol emission parameters weakens ΔF_{aci} (less negative) everywhere. However, *sea_salt* has a strong influence on global mean ΔF_{aci} uncertainty due to its influence in the NH, whilst *dms* is most important in the south-eastern Pacific coastal region. The *dms* parameter affects secondary aerosol formation and particle growth, so causes more remaining ΔF_{aci} uncertainty in this relatively polluted region with high present-day aerosol concentrations. The aerosol removal parameter 510 *dry_dep_acc* also causes around 14 % of the remaining ΔF_{aci} uncertainty. This parameter is most important in regions of outflow from anthropogenic pollution sources. Increasing aerosol removal rates in these regions strengthens annual mean ΔF_{aci} (more negative) by reducing baseline aerosol concentrations which makes clouds more susceptible to aerosol changes (Carslaw et al., 2013), though the sign of this effect varies across seasons (Regayre et al., 2015). Additionally, the parameter controlling 515 turbulent entrainment, *a_ent_1_rp*, causes around 9 % of the remaining ΔF_{aci} uncertainty, with the largest contributions in marine regions associated with stratocumulus to cumulus transition. Increasing the

21

entrainment rate weakens ΔF_{aci} (less negative) in these regions by reducing cloud amount and thus susceptibility to aerosol changes.

520   The sign of ΔF_{aci} dependence on parameter perturbations can vary between regions. This indicates that changing a parameter value strengthens ΔF_{aci} in some regions but weakens it in others. For example, there is a clear boundary between Eastern and Western China, where the dependence of ΔF_{aci} on several physical atmosphere parameters changes sign (*bparam*, *two_d_fsd_factor*, *c_r_correl*, *autoconv_exp_lwp*, *dbsdtbs_turb_0*, *a_ent_1_rp*). These sign changes are also evident within some ocean

525   basins (e.g. *dbsdtbd_turb_0* and *m_ci* in the South Pacific; *two_d_fsd_factor* in the North Atlantic). Furthermore, the change in sign of ΔF_{aci} dependence on physical atmosphere parameters aligns spatially with the influence of the parameter controlling black carbon radiative properties (*bc_ri*). For example, this parameter is the dominant cause of ΔF_{aci} uncertainty in central China (more than 30 %) yet contributes relatively little to ΔF_{aci} uncertainty in neighbouring Chinese regions (around 10 %). We hypothesise the

530   sign of ΔF_{aci} dependence on physical atmosphere parameters is determined by the effect of the *bc_ri* parameter, which determines the importance of physical atmosphere parameters by affecting boundary layer stability and cloud properties including cloud depth (Bond et al., 2013; Zhuang et al., 2010).

        Non-uniform regional variation in the parameters causing ΔF_{aci} uncertainty means that global mean

535   ΔF_{aci} is resistant to the type of broad regional mean observational constraints applied by R23. That is, comparing regional mean model output to observations sub-optimally combines smaller-scale variations in ΔF_{aci} dependence on uncertain model parameters. Thus, this analysis of remaining ΔF_{aci} uncertainty at the model grid box scale provides new insight into how observational constraints can be calculated and applied. In the following section, we take this analysis further by clustering the data according to shared

540   causes of remaining ΔF_{aci} uncertainty rather than by geographical region. Theoretically, further ΔF_{aci} constraint could be achieved using targeted observations within these clusters of shared causes of uncertainty (Lee et al., 2016).

3.4 Regional clusters of remaining ΔF_{aci} uncertainty and observations to constrain them

In this section, we explore how clustering regions according to their shared causes of remaining ΔF_{aci} uncertainty can inform future strategies for further observational constraint.

In Fig. 4 we cluster the combinations of parameters that cause unconstrained and remaining ΔF_{aci} uncertainty (see also Appendix A Fig. A4 - a similar map for the original ΔF_{aci} uncertainty). Each cluster is concentrated in regions determined by the importance of locally dominant processes. Neighbouring clusters typically share one or more important parameters, which suggest causes of ΔF_{aci} uncertainty vary systematically across regions defined by these clusters. Spatial coverage of some clusters is reduced by the optimal constraint. Coverage is reduced by at least 75 % for the 2nd (orange) and 8th (grey) clusters and by around 50 % for the 3rd (green) cluster after optimal constraint. Reduced spatial coverage of these clusters (across continental Europe and North America, and high latitude marine regions) suggests combinations of parameters associated with them are constrained by R23 in certain areas. However, the persistence of these clusters in other regions suggests ΔF_{aci} dependence on model parameters is not uniform within clusters. This may be due to interactions with other uncertain parameters or regional differences in how parameters affect ΔF_{aci}.
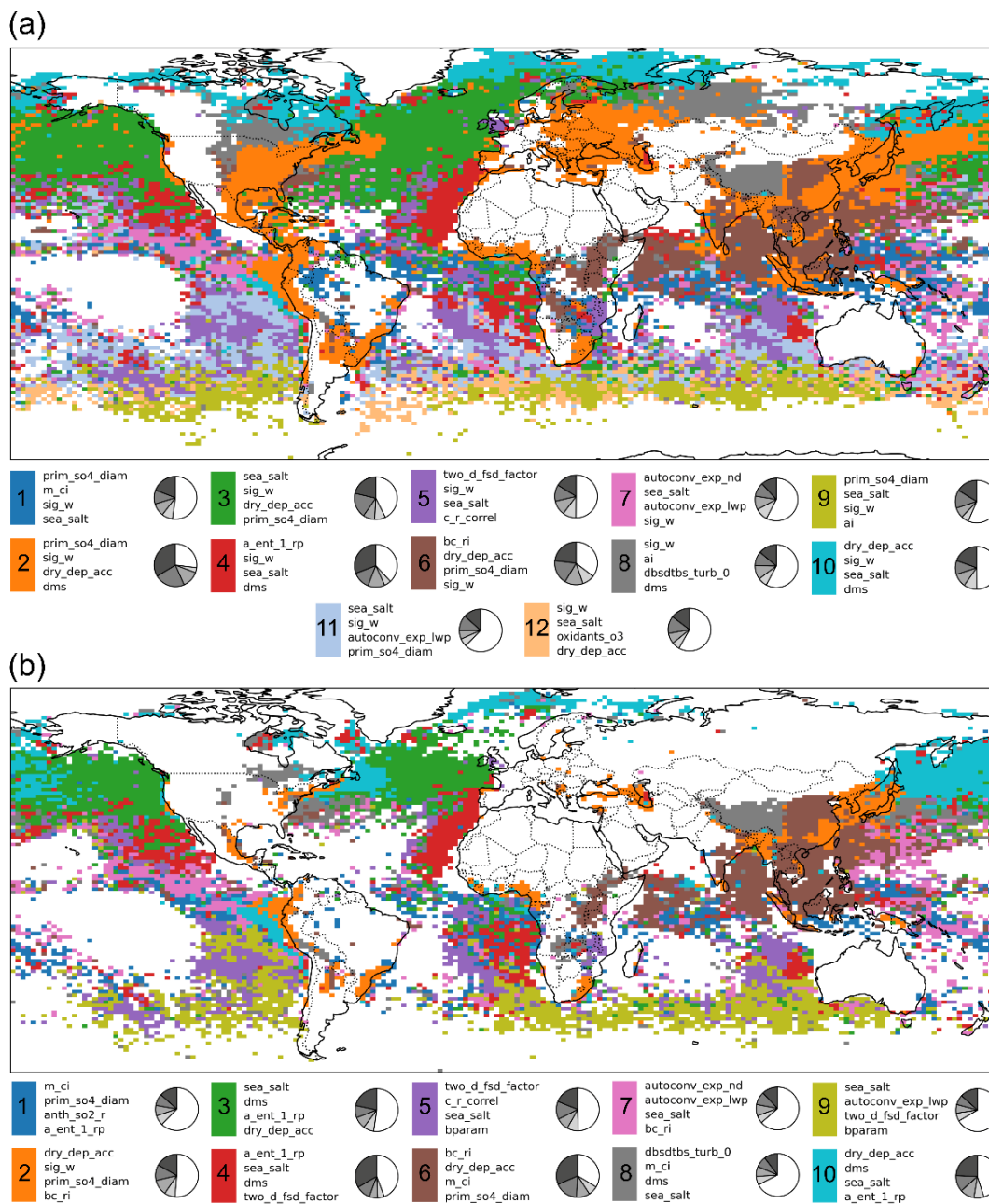
(a)

(b)

Fig. 4. Maps of shared causes of remaining ΔF_{aci} uncertainty, a) in the unconstrained set of model variants (the 90 % of the original 1 million with prim_so4_diam parameter values larger than 10 nm; Section 2.4), and b) after R23 optimal constraint. Model grid boxes where remaining ΔF_{aci} uncertainty is less than 0.5 W m^{-2} are masked. The legend shows the 4 most important causes of uncertainty in each cluster and counter-clockwise shading in the pie charts shows the corresponding proportions of uncertainty caused by these parameters, out of 100 % total, with the white region representing contributions from the other 33 parameters.

24

Fig. 5 shows how progressively adding observations to the optimal constraint affects causes of ΔF_{aci}

uncertainty in each cluster (Fig. 4). The cloud droplet activation parameter (*sig_w*) and primary sulfate

parameter (*prim_so4_diam*) are constrained by more than 50 % in most clusters. However, other

parameters are not strongly constrained and therefore cause a similar or higher proportion of remaining

ΔF_{aci} uncertainty after constraint. The persistence of key causes of ΔF_{aci} uncertainty in each region, even

as the overall uncertainty is reduced, suggests that the R23 constraint only partially constrains the

governing processes. A deeper understanding of how these parameters interact with other causes of ΔF_{aci}

uncertainty at the regional level is needed to inform further constraint efforts.
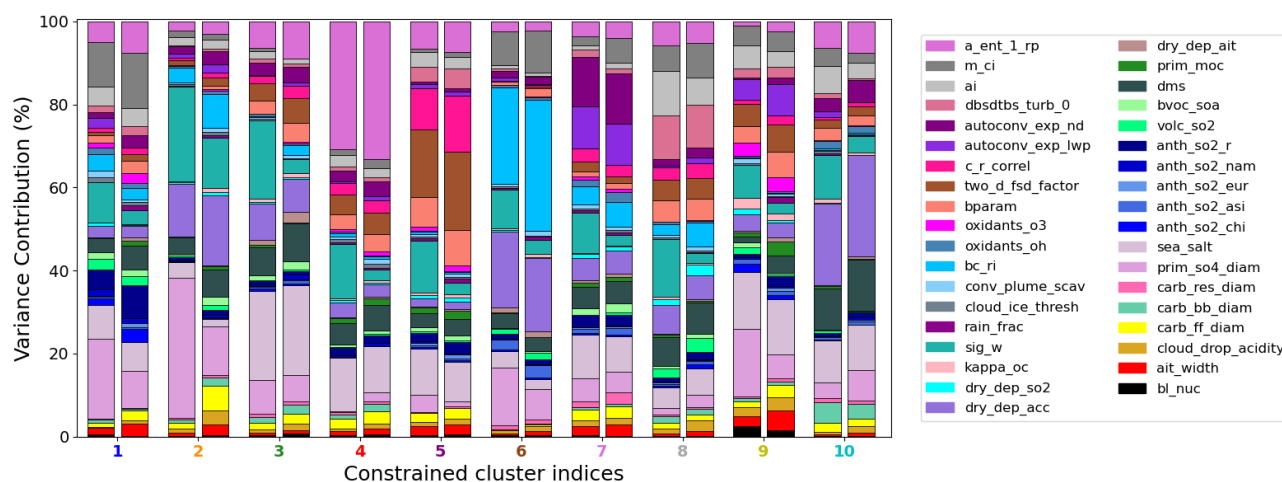
Fig. 5. Proportion of ΔF_{aci} variance caused by the 37 parameters in the first 10 unconstrained (left) and all 10 optimally constrained (right) clusters (indexed in Fig. 4). Cluster indices and colors on the x-axis match Fig. 4. Parameter contributions to ΔF_{aci} variance are shown in consistent order for each bar, though near-zero contributions are not always visible.

Our analysis of remaining ΔF_{aci} uncertainty focusses on clusters where ΔF_{aci} is resistant to the R23

constraint (Fig. 2), beginning with Asia, where ΔF_{aci} uncertainty is weakly constrained (less than 30 %)

so remains greater than 10 W m^{-2}. Asia is partitioned into three clusters of remaining uncertainty (2:

orange, 6: brown and 8: grey). In section 3.3, we described how the parameter controlling the refractive

index of carbonaceous aerosol (*bc_ri*) can affect the atmospheric state and thus the sign of ΔF_{aci}

590 dependence on some physical atmosphere parameters (Fig. 3). The *bc_ri* parameter is particularly important in Cluster 6 (brown) where in combination with the dry deposition parameter (*dry_dep_acc*) it causes nearly 50 % of the remaining ΔF_{aci} uncertainty. This cluster extends into the Indian Ocean, East China Sea and western Pacific. The two main causes of remaining ΔF_{aci} uncertainty in this cluster (deposition processes and aerosol optical properties) also represent major sources of multi-model

595 diversity in aerosol optical depth over biomass burning regions (Petrenko et al., 2025). In theory, available measurements of carbonaceous aerosol optical properties within this cluster over Asia (e.g. Budhavant et al., 2024; Sun et al., 2024) should further reduce regional ΔF_{aci} uncertainty by up to 35 %. However, observed variability in optical properties, driven by differences in aerosol mixing state (Bond et al., 2013; Fierce et al., 2016; Lack and Cappa, 2010), is not well represented in climate models. It is difficult to

600 attribute radiative effects to individual species using climate models because aerosol species are typically treated as internally mixed (mixing state assumptions; e.g. Sand et al., 2021). As a result, observational constraints based on in-situ data may not be representative of the entire cluster, particularly across multiple regions. In such cases, region-specific observational constraints may be needed to constrain the cluster contribution to global mean ΔF_{aci} uncertainty.

605 Over densely populated and industrialized regions of Asia (Cluster 2, orange; spanning India, China's coast, Indonesia, Japan and Korea) the remaining uncertainty in ΔF_{aci} is dominated by dry deposition (*dry_dep_acc*), cloud droplet activation (*sig_w*) and primary sulfate emission properties (*prim_so4_diam*). The importance of updraft velocity in these regions is consistent with an updraft-limited regime of cloud droplet activation when aerosol concentrations are high (Reutter et al., 2009). It

610 is essential to constrain ΔF_{aci} uncertainty in updraft-limited regimes because the sensitivity of cloud properties to aerosol under these conditions shapes our understanding of future climate responses (Andersen et al., 2023; Jia and Quaas, 2023).

Cluster 2 (orange), most dominant over Asia, spans several other industrial zones, including the coasts of North and South America, Africa, and the Mediterranean, so constraint of the combined

615 parameter effects on ΔF_{aci} in any of these regions could reduce uncertainty more widely unless these three parameters have regionally specific values (currently not assumed in the model). Opportunities for

widespread constraint of uncertainty in Cluster 2 may be found through existing observations. For example, additional ΔF_{aci} constraint beyond R23 might be achieved using in-situ sulfate concentration and aerosol deposition measurements from Japanese EANET (Acid Deposition Monitoring Network in

620 East Asia) stations (Endo et al., 2011) in combination with extensive in-situ concentration and size distribution observations collected as part of the Aerosol Characterization Experiments (ACE) Asia (Huebert et al., 2003). Over Peru and Ecuador, where remaining uncertainty exceeds 5 W m^{-2} (Fig. 2c), the relevant observations are currently lacking so far as we are aware. While the VOCALS campaign (Wood et al., 2011) measured atmospheric properties within our Cluster 2, aerosol data were only

625 collected further south. Other campaigns in our target region measure deposition fluxes (e.g. Baker et al., 2016) but focus on metal deposition as a source of marine biogenic activity, so are not suitable for broader climate model constraint. The lack of suitable observations in this region highlights a specific opportunity: novel measurements using, for example, condensation particle counters (for aerosol concentration data), mobility particle size spectrometers (for aerosol size distributions) and deposition

630 collectors (removal rates) at specific coastal sites aligned to prevailing wind direction could play a critical role in reducing ΔF_{aci} uncertainty.

Remaining uncertainty over the North Pacific and North Atlantic Oceans share four main clusters: in the west nearest to outflowing anthropogenic pollution it is Cluster 2 (orange), immediately downwind it is Cluster 10 (cyan), which transitions into Cluster 3 (green) and ultimately Cluster 4 (red)

635 on the eastern side of each NH ocean basin. Although R23 constrained ΔF_{aci} uncertainty by more than 70 % in NH marine regions (Fig. 2d), the uncertainty remains greater than 3 W m^{-2} (Fig. 2c). The aerosol deposition parameter (*dry_dep_acc*) causes nearly 25 % of the remaining ΔF_{aci} uncertainty in Cluster 10 (cyan), with more than 10% each from natural aerosol emission parameters (*dms* and *sea_salt*) and around 10 % from the parameter controlling turbulent cloud top entrainment

640 (*a_ent_1_rp*). The importance of aerosol removal (*dry_dep_acc*) decreases to less than 10 % in Cluster 3 (green) and less than 5 % in Cluster 4 (red). In contrast, the cloud top entrainment parameter (*a_ent_1_rp*) increases in importance further from anthropogenic emission sources, causing around 10 % of the remaining ΔF_{aci} uncertainty in Cluster 3 (green) and around 35 % in Cluster 4 (red) where

remaining uncertainty is greatest (larger than 5 W m^{-2}). In the central Cluster 3 (green) which covers

645   most of the NH mid-Atlantic and mid-Pacific regions, sea salt emissions (*sea_salt*) and dimethylsulfide

emissions (*dms*) combine to cause more than 25 % of the remaining uncertainty.

These results suggest ΔF_{aci} could be further constrained over NH ocean regions using existing

observations that target each cluster. For example, extensive aerosol, cloud and radiation measurements

from the Department of Energy Atmospheric Radiation Measurement (ARM) site on Graciosa Island

650   (Mather and Voyles, 2013; Zheng et al., 2018) and associated Eastern North Atlantic flight campaign

(ACE-ENA; Wang et al., 2022; Yeom et al., 2021) may help reduce ΔF_{aci} uncertainty associated with

cloud top entrainment (parameter *a_ent_1_rp*) and natural aerosol emissions (*dms* and *sea_salt*) in

Cluster 4 (red). These measurements could be complemented by sea salt mass concentration

measurements from Atmospheric Tomography (ATom) missions (Brock et al., 2022), which span

655   Clusters 3 (green) and 4 (red) across both the North Pacific and North Atlantic (e.g. Murphy et al.,

2019), and aerosol concentration and size distribution measurements from the North Atlantic Aerosols

and Marine Ecosystems Study (NAAMES) in Cluster 10 (cyan) within the western North Atlantic

(Gallo et al., 2023).

There is a contrast between clusters of ΔF_{aci} uncertainty in NH and SH marine regions. Cluster 3

660   (green) is less prominent in the SH, where Cluster 5 (purple) features in each ocean basin, accompanied

by Cluster 9 (yellow) and, except in the South Pacific, Cluster 4 (red). ΔF_{aci} uncertainty is only weakly

constrained (by 40 % or less) in these regions (Fig. 2d). In each of these clusters, the dominant

parameter is the one controlling how the spatial distribution of clouds affects radiation within model

grid boxes (*two_d_fsd_factor*), causing around 20 % of the remaining ΔF_{aci} uncertainty in Cluster 5 and

665   around 10 % in other clusters. Additional contributors to remaining uncertainty include the cloud-

precipitation overlap parameter (*c_r_correl*; around 15 % in Cluster 5) and an autoconversion

sensitivity parameter (*autoconv_exp_lwp*; more than 5 % in Cluster 9). The importance of these

physical atmosphere model parameters suggests a need to constrain the transition from stratocumulus to

cumulus clouds, which might be achieved using process-based observations, such as co-varying aerosol

670   and cloud properties (e.g. Gryspeerdt et al., 2016), subject to addressing discrepancies between models

and satellite data (Kokkola et al., 2025; Quaas et al., 2020). However, model structural deficiencies have thus far prevented observed cloud properties associated with these physical atmosphere parameters being used as constraints (Regayre et al., 2023). In practice, model developments informed by large eddy simulation analyses (e.g. Sansom et al., 2024) may be needed to improve cloud transitions in
675   global climate models and further constrain ΔF_{aci} uncertainty in SH marine regions.

4   Conclusions

The Regayre et al. (2023) optimal constraint reduced global annual mean ΔF_{aci} uncertainty by nearly 70 % (90 % credible interval spanning -0.9 to -0.1 W m^{-2}). However, our results here show that the observational constraint did not affect all regions (Fig. 2d) or causes of uncertainty (Fig. 5) equally.
680   Although the uncertainty caused by the two main drivers of original ΔF_{aci} uncertainty, parameters controlling the diameter of primary sulfate particles (*prim_so4_diam*) and cloud droplet activation (cloud updraft speed; *sig_w*), is greatly reduced, all other parameters cause a similar or greater proportion of remaining uncertainty (Fig. 5 and Appendix A Table A2). Remaining ΔF_{aci} uncertainty is greatest in continental Asia (90 % credible interval greater than 10 W m^{-2}) and SH regions of persistent stratocumulus
685   cloud (5 to 10 W m^{-2}; Fig. 2c).

By analyzing clusters of shared causes of remaining ΔF_{aci} uncertainty (Fig. 4), we identify specific existing observational data likely to further constrain ΔF_{aci} in our model (Table 1). However, observations related to key causes of uncertainty are not available across all regions and clusters. For example, novel
690   observations of aerosol species concentrations, size distributions and deposition fluxes at multiple sites along the coasts of Peru and Ecuador would be highly valued for their potential to further constrain ΔF_{aci} in Cluster 2 (orange) which would have a broad impact on remaining uncertainty in other regions of persistent uncertainty. These results show how evaluating models within an uncertainty framework can identify novel observations which, if made, would likely provide far-reaching additional constraint of
695   ΔF_{aci}.

700   Table 1: Summary of existing observations with high potential to further constrain ΔF_{aci}, and the processes they would target

Cluster(s)	Key observation data	Source(s)	Spatial extent of cluster(s)	Target causes of remaining ΔF_{aci}, uncertainty
Brown: 6	Carbonaceous aerosol optical properties	Budhavant et al., (2024); Sun et al., (2024)	Central China, SE Asia, Indian Ocean, NW Pacific	bc_ri; dry_dep_acc
Orange: 2	Species concentrations; Aerosol deposition; Aerosol size distribution	EANET - Endo et al., (2011); ACE-Asia - Huebert et al., (2003)	Eastern China, India, Industrialized coastal regions	dry_dep_acc; sig_w; prim_so4_diam
Cyan: 10	Species concentrations, Aerosol size distribution	NAAMES - Gallo et al., (2023)	NW Pacific, NW Atlantic, SE Pacific, Arctic	dry_dep_acc; sea_salt; dms
Green: 3	Sea salt concentrations	ATom - Brock et al., (2022); Murphy et al., (2019)	North Pacific, North Atlantic	sea_salt; dms; dry_dep_acc
Red: 4	Aerosol number concentration, Aerosol size distribution, Cloud and aerosol vertical and radiative properties	ARM (Graciosa Island) - Mather and Voyles (2013); Zheng et al. (2018); ARM-ENA - Wang et al. (2022); Yeom et al. (2021)	NE Atlantic, NE Pacific, SE Atlantic; SE Indian	a_ent_1_rp
Purple: 5 and Yellow: 9	Co-varying aerosol and cloud properties	Gryspeerdt et al. (2016)	Southern Hemisphere marine regions	two_d_fsd_factor; c_r_correl; autoconv_exp; sea_salt

The conventional approach to model development typically focusses on increasing model fidelity, often inspired by the detection of biases or insights from multi-model intercomparisons (Chen et al.,
705   2021). However, apparent improvements in model skill can largely be attributed to parameter retuning rather than genuine structural advances (Rostron et al., 2025). Increasing model fidelity carries a computational burden which is not always beneficial (Proske et al., 2022). Operationalizing a more

targeted model development cycle requires structural modifications, evaluation within an uncertainty framework (Lee et al., 2012; Sexton et al., 2021), and successive waves of observational constraint to reduce model uncertainty and reveal structural deficiencies (Elsaesser et al., 2025; Fierce et al., 2024; Johnson et al., 2020; McNeall et al., 2016; Regayre et al., 2023). Diagnosing the causes of remaining uncertainty, as demonstrated here, is a key step in this cycle.

Here we have described a workflow for constraining (narrowing uncertainty in) aerosol radiative forcing that combines perturbed parameter ensembles (PPEs), extensive observational constraints and statistical analyses to track changes in the causes of uncertainty as observational constraints are progressively applied. Systematically analyzing the causes of remaining ΔF_{aci} uncertainty after observational constraint enables us to: a) identify regions where model uncertainty resists observational constraint (highlighting *where* additional observational data are most needed) and b) partition regions into clusters of shared uncertainty sources (pointing to existing and novel *observation types* that could further reduce ΔF_{aci} uncertainty). Our analysis also suggests model uncertainty may be more effectively constrained if observational constraints were applied *within clusters* of common causes of model uncertainty, rather than across geographic regions that are likely to span multiple clusters. This approach to model evaluation and constraint provides actionable information to guide both further observational constraint and efforts to increase model fidelity that directly target ΔF_{aci} uncertainty.

The workflow of progressive observational constraint and clustering of the common causes of uncertainty demonstrated here tackles only part of the overall uncertainty in aerosol radiative forcing – parametric uncertainty. The other part, highlighted by R23, is structural uncertainty caused by structural deficiencies in models. Progressive observational constraint, reclustering, identification of new target observations and further constraint only works if the multiple observations provide *consistent* constraints on the uncertain parameters, but R23 showed that inconsistency is likely to become a problem even after very few constraints have been applied – that is, different observations constrain the model to different (inconsistent or non-overlapping) parts of parameter space. As we outlined in R23, the approach we have shown here would therefore need to be combined with efforts to address these inconsistencies by making

model structural improvements. We suggest that targeting model development at the processes causing such multi-variable inconsistency will be more efficient than addressing causes of bias in single variables.

A key question is how transferable ΔF_{aci} constraint derived from a single model is to other models. While climate models share multiple parameterisations and fundamental assumptions, and are evaluated against similar observational datasets (Knutti et al., 2013; Kuma et al., 2023; Sanderson et al., 2015), differences in tuning strategies (Hourdin et al., 2017) and configurations result in diverse responses to anthropogenic aerosol changes (Bellouin et al., 2020; Intergovernmental Panel On Climate Change, 2023). To ensure our approach supports improvements across a range of climate models, it is essential to extend this development and evaluation cycle across multiple models. Multi-model PPEs (MM-PPEs), which simultaneously sample both structural and parametric uncertainties, offer a more robust basis for identifying structural deficiencies, targeting model development priorities, and guiding future observation strategies. Applying our approach systematically across different models and model versions would build a foundation for strategic, evidence-based climate model development.

Appendix A

Additional figures A1 to A4 and Tables A1, A2.
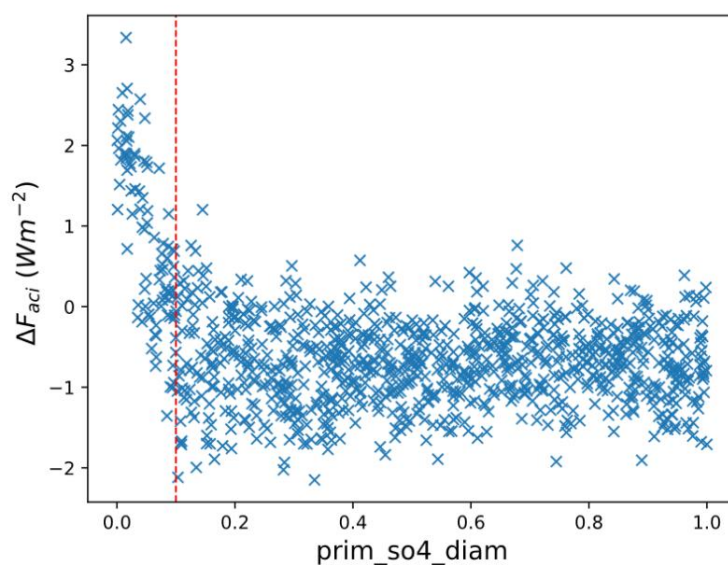
Fig. A1. The marginal dependence of ΔF_{aci} on normalized prim_so4_diam parameter values. Values for the first 1 000 of the

755   original 1 million model variants are shown. Parameter values are normalized to be on the 0-1 scale. The dashed line separates

values below around 10 nm, which were removed to create Fig. 2b) and the set of model variants referred to as unconstrained.
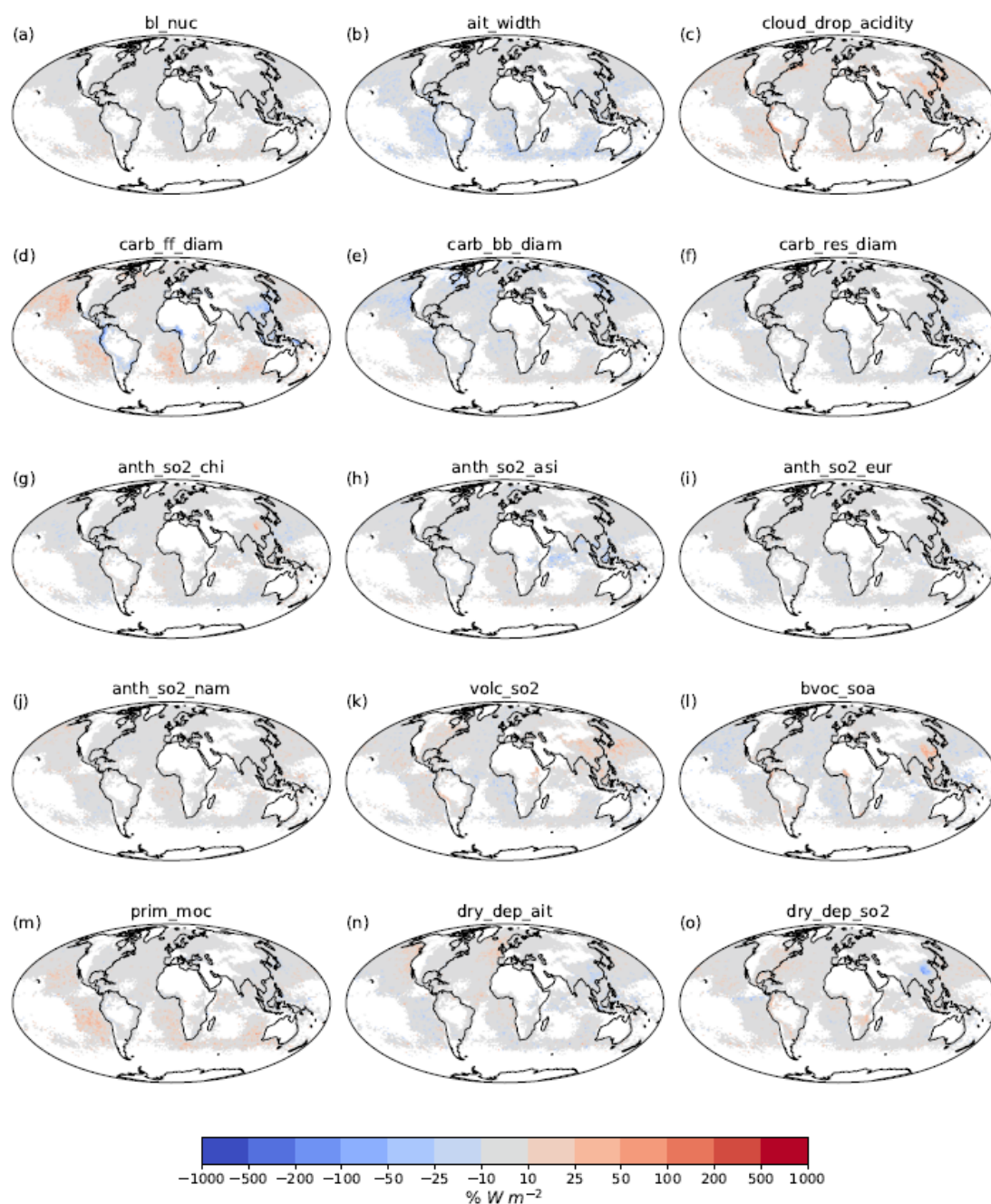
Fig. A2. Maps of parametric causes of remaining ΔF_{aci} uncertainty after optimal constraint for 15 of the 22 parameters not shown in Fig. 3. Shading indicates the proportion of variance caused by individual parameters, multiplied by the variance in that grid box and by the sign of the ΔF_{aci} dependence on the parameter value. Negative values indicate increasing the parameter value is associated with stronger (more negative) ΔF_{aci} values. Regions where the ΔF_{aci} 90 % CI is less than 3 W m^{-2} are masked.
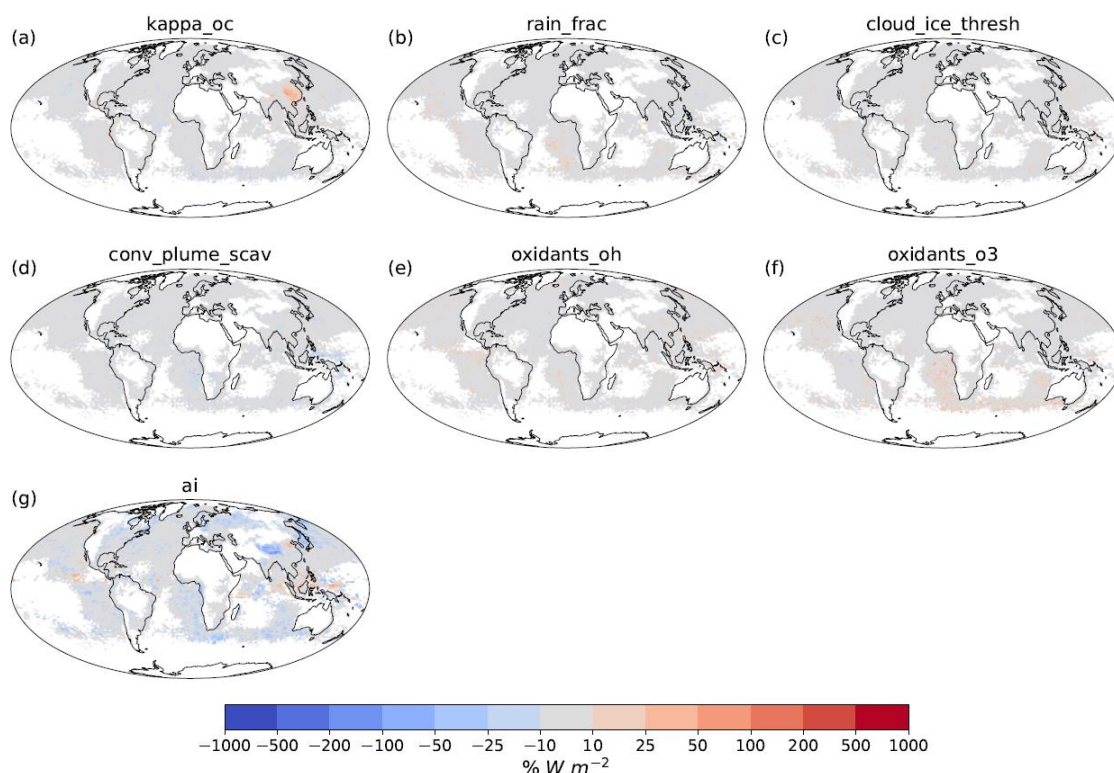
Fig. A3. Maps of parametric causes of remaining ΔF_{aci} uncertainty after optimal constraint for the 7 parameters not shown in Fig. 3 nor Fig. A2. Shading indicates the proportion of variance caused by individual parameters, multiplied by the variance in that grid box and by the sign of the ΔF_{aci} dependence on the parameter value. Negative values indicate increasing the parameter value is associated with stronger (more negative) ΔF_{aci} values. Regions where the ΔF_{aci} 90 % CI is less than 3 W m^{-2} are masked.
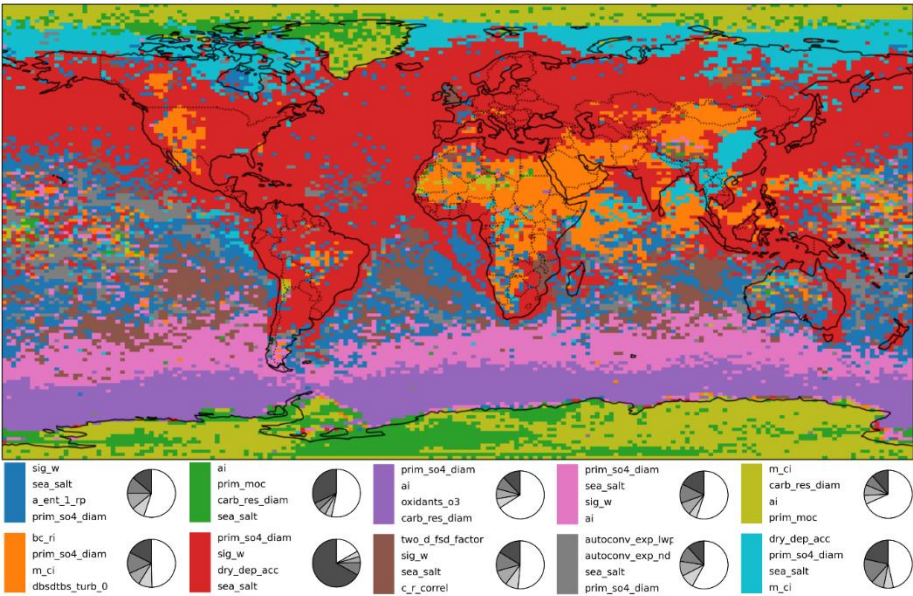
Fig. A4. Shared causes of ΔF_{aci} uncertainty in the original set of 1 million model variants. As with Fig. 4 in the main article, the legend shows the 4 most important causes of uncertainty in each cluster and clockwise shading in the pie charts shows the corresponding proportions of uncertainty caused by these parameters, out of 100% total, with the white region representing contributions from the other 33 parameters.

Table A1. Parameter names, perturbation type and description, following Regayre et al., (2023).

Parameter name	Perturbation type	Description
bl_nuc	Aerosol process	Boundary layer nucleation rate scale factor
ait_width	Aerosol process	Modal width of Aitken modes
cloud_drop_acidity	Aerosol process	Cloud droplet acidity
carb_ff_diam	Aerosol process	Emission diameter of carbonaceous aerosol from fossil fuel sources
carb_bb_diam	Natural aerosol emission	Emission diameter of carbonaceous aerosol from biomass burning sources
carb_res_diam	Anthropogenic aerosol emission	Emission diameter of carbonaceous aerosol from residential sources

prim_so4_diam	Anthropogenic aerosol emission	Emission diameter of 50% of new sub-grid sulfate particles. Remaining 50% emitted into the larger coarse mode
sea_salt	Natural aerosol emission	Sea salt emission flux scale factor
anth_so2_chi	Anthropogenic aerosol emission	Anthropogenic SO_2 emission flux scale factor – China
anth_so2_asi	Anthropogenic aerosol emission	Anthropogenic SO_2 emission flux scale factor – Asia
anth_so2_eur	Anthropogenic aerosol emission	Anthropogenic SO_2 emission flux scale factor – Europe
anth_so2_nam	Anthropogenic aerosol emission	Anthropogenic SO_2 emission flux scale factor - North America
anth_so2_r	Anthropogenic aerosol emission	Anthropogenic SO_2 emission flux scale factor - Rest of the world
volc_so2	Natural aerosol emission	Volcanic SO_2 emission flux scale factor
bvoc_soa	Natural aerosol emission	Biogenic monoterpene production rate of secondary organic aerosol scale factor
dms	Natural aerosol emission	Dimethyl-sulfide emission flux scale factor
prim_moc	Natural aerosol emission	Primary marine organic carbon emission flux scale factor
dry_dep_ait	Aerosol process	Dry deposition velocity of Aitken mode aerosol
dry_dep_acc	Aerosol process	Dry deposition velocity of accumulation mode aerosol
dry_dep_so2	Aerosol process	Dry deposition velocity of SO_2
kappa_oc	Aerosol process	Hygroscopicity parameter (κ) for organic aerosol – affects wet diameter and clear-sky radiative flux
sig_w	Aerosol process	Standard deviation of shallow-cloud updraft velocity scale factor
rain_frac	Aerosol process	Fraction of cloud covered area where rain removes aerosol
cloud_ice_thresh	Aerosol process	Threshold of cloud ice water fraction for scavenging
conv_plume_scav	Aerosol process	Scavenging efficiency (as a fraction of total aerosol removed) of Aitken mode aerosol in convective clouds
bc_ri	Aerosol process	Imaginary part of the black carbon refractive index
oxidants_oh	Aerosol process	Offline oxidant OH concentration scale factor
oxidants_o3	Aerosol process	Offline oxidant O_3 concentration scale factor
bparam	Physical atmosphere	Coefficient of the spectral shape parameter (β) for effective radius

two_d_fsd_factor	Physical atmosphere	Scale factor for the 2D relationship between cloud condensate variance, cloud cover and convection - Controls sub-grid cloud heterogeneity
c_r_correl	Physical atmosphere	Cloud and rain sub-grid horizontal spatial colocation
autoconv_exp_lwp	Physical atmosphere	Exponent of liquid water path in the power law for initiating autoconversion
autoconv_exp_nd	Physical atmosphere	Exponent of cloud droplet concentration (N_d) in the power law for initiating autoconversion
dbsdtbs_turb_0	Physical atmosphere	Cloud erosion rate
ai	Physical atmosphere	Scaling coefficient for the dependence of ice mass on diameter
m_ci	Physical atmosphere	Ice fall speed scale factor
a_ent_1_rp	Physical atmosphere	Cloud top entrainment rate scale factor

Table A2. Percentage of ΔF_{aci} uncertainty (90 % credible interval) caused by each of the 37 perturbed parameters before, during and after optimal constraint. In the original set, causes of variance greater than 2 % of the total are in bold font, indicating these parameters are in the first ΔF_{aci} bar in Fig. 1. Causes of remaining variance after the 13th (optimal) constraint are also
785 bold where they differ from the original causes by more than 1 %

Parameter	Original (1 million)	Un-constrained (900 000)	After 1st constraint (431 143)	After 2nd constraint (75 936)	After 4th constraint (5 000)	After 13th (optimal) constraint (5 000)
bl_nuc	0.0	0.0	0.0	0.0	0.0	0.0
ait_width	0.6	1.4	1.5	2.3	2.9	**2.8**
cloud_drop_acidity	0.4	0.9	1.0	1.4	1.6	**1.5**
carb_ff_diam	0.5	1.0	0.9	1.3	1.1	1.4
carb_bb_diam	0.1	0.2	0.3	0.4	0.5	0.5
carb_res_diam	0.1	0.1	0.2	0.2	0.3	0.2
prim_so4_diam	**54.9**	3.5	26.0	10.4	5.0	**2.8**
sea_salt	**7.4**	17.0	12.4	14.4	16.3	**17.0**
anth_so2_chi	0.1	0.2	0.2	0.3	0.3	0.3
anth_so2_asi	0.0	0.1	0.1	0.2	0.3	0.3
anth_so2_eur	0.0	0.0	0.0	0.0	0.0	0.0

anth_so2_nam	0.0	0.0	0.0	0.1	0.2	0.2
anth_so2_r	0.8	1.9	1.8	2.7	3.2	**3.0**
volc_so2	0.2	0.5	0.7	0.9	1.2	1.1
bvoc_soa	0.0	0.0	0.0	0.0	0.0	0.0
dms	**3.5**	8.1	7.8	8.9	12.5	**12.3**
prim_moc	0.1	0.4	0.3	0.5	0.5	0.6
dry_dep_ait	0.0	0.0	0.0	0.0	0.0	0.0
dry_dep_acc	**6.0**	13.6	13.6	13.1	10.8	**14.4**
dry_dep_so2	0.1	0.4	0.3	0.6	0.7	0.7
kappa_oc	0.1	0.2	0.1	0.2	0.2	0.2
sig_w	**13.9**	25.6	10.8	7.9	5.3	**5.1**
rain_frac	0.0	0.0	0.0	0.0	0.0	0.0
cloud_ice_thresh	0.1	0.3	0.2	0.4	0.5	0.4
conv_plume_scav	0.2	0.2	0.2	0.3	0.3	0.3
bc_ri	0.8	1.6	1.5	2.4	2.7	**2.7**
oxidants_oh	0.1	0.1	0.1	0.2	0.2	0.2
oxidants_o3	0.0	0.0	0.0	0.1	0.1	0.1
Bparam	1.0	2.2	2.1	3.1	3.5	**3.3**
two_d_fsd_factor	1.6	3.7	3.4	5.3	5.5	**5.6**
c_r_correl	0.6	1.5	1.3	2.1	2.5	**2.5**
autoconv_exp_lwp	0.3	0.7	0.8	1.1	1.3	1.1
autoconv_exp_nd	1.2	2.4	2.4	3.4	3.9	**3.8**
dbsdtbs_turb_0	0.5	1.2	1.2	1.8	2.1	**2.1**
ai	1.7	3.6	3.4	4.8	4.1	**3.2**
m_ci	0.3	0.8	0.7	1.1	1.3	1.2
a_ent_1_rp	**2.8**	6.2	4.9	8.2	8.9	**9.0**

Code availability

Code used to create figures in this article are available here: https://doi.org/10.5281/zenodo.16686812

790 (Regayre, 2025)

Data availability

Output from the A-CURE PPE is available on the CEDA archive (Regayre *et al.*, 2022).

Author contributions

795 LR led the research, processed output from the ensemble, created statistical emulators, and implemented GAM analyses at the model grid box level, building on historical input from JJ. LR and KC wrote the article with contributions from all co-authors. JOa, JJ, JOw, and KG provided valuable recommendations regarding statistical analyses, and all co-authors contributed to the development of the methodology. LP created the K-means clusters with input from LR. The research was motivated by concepts stemming 800 from collaborative discussions among all co-authors, with KC providing overarching vision and guidance.

Competing interests

At least one of the (co-)authors is a member of the editorial board of Atmospheric Chemistry and Physics.

Acknowledgements

References

Albrecht, B. A.: Aerosols, Cloud Microphysics, and Fractional Cloudiness, Science, 245, 1227–1230,
https://doi.org/10.1126/science.245.4923.1227, 1989.

Andersen, H., Cermak, J., Douglas, A., Myers, T. A., Nowack, P., Stier, P., Wall, C. J., and Wilson Kemsley, S.: Sensitivities
of cloud radiative effects to large-scale meteorology and aerosols from global observations, Atmos. Chem. Phys., 23, 10775–
10794, https://doi.org/10.5194/acp-23-10775-2023, 2023.

Andres, R. J. and Kasgnoc, A. D.: A time-averaged inventory of subaerial volcanic sulfur emissions, J. Geophys. Res., 103,
25251–25261, https://doi.org/10.1029/98JD02091, 1998.

Archibald, A. T., O'Connor, F. M., Abraham, N. L., Archer-Nicholls, S., Chipperfield, M. P., Dalvi, M., Folberth, G. A.,
Dennison, F., Dhomse, S. S., Griffiths, P. T., Hardacre, C., Hewitt, A. J., Hill, R. S., Johnson, C. E., Keeble, J., Köhler, M. O.,
Morgenstern, O., Mulcahy, J. P., Ordóñez, C., Pope, R. J., Rumbold, S. T., Russo, M. R., Savage, N. H., Sellar, A., Stringer,
M., Turnock, S. T., Wild, O., and Zeng, G.: Description and evaluation of the UKCA stratosphere–troposphere chemistry
scheme (StratTrop vn 1.0) implemented in UKESM1, Geosci. Model Dev., 13, 1223–1266, https://doi.org/10.5194/gmd-13-
1223-2020, 2020.

Baker, A. R., Thomas, M., Bange, H. W., and Plasencia Sánchez, E.: Soluble trace metals in aerosols over the tropical south-
east Pacific offshore of Peru, Biogeosciences, 13, 817–825, https://doi.org/10.5194/bg-13-817-2016, 2016.

Balkanski, Y., Schulz, M., Claquin, T., and Guibert, S.: Reevaluation of Mineral aerosol radiative forcings suggests a better
agreement with satellite and AERONET data, Atmos. Chem. Phys., 7, 81–95, https://doi.org/10.5194/acp-7-81-2007, 2007.

Bellouin, N., Quaas, J., Morcrette, J.-J., and Boucher, O.: Estimates of aerosol radiative forcing from the MACC re-analysis,
Atmos. Chem. Phys., 13, 2045–2062, https://doi.org/10.5194/acp-13-2045-2013, 2013.

Bellouin, N., Quaas, J., Gryspeerdt, E., Kinne, S., Stier, P., Watson-Parris, D., Boucher, O., Carslaw, K. S., Christensen, M.,
Daniau, A. -L., Dufresne, J. -L., Feingold, G., Fiedler, S., Forster, P., Gettelman, A., Haywood, J. M., Lohmann, U., Malavelle,
F., Mauritsen, T., McCoy, D. T., Myhre, G., Mülmenstädt, J., Neubauer, D., Possner, A., Rugenstein, M., Sato, Y., Schulz,
M., Schwartz, S. E., Sourdeval, O., Storelvmo, T., Toll, V., Winker, D., and Stevens, B.: Bounding Global Aerosol Radiative
Forcing of Climate Change, Rev. Geophys., 58, https://doi.org/10.1029/2019RG000660, 2020.

Beven, K. and Freer, J.: Equifinality, data assimilation, and uncertainty estimation in mechanistic modelling of complex environmental systems using the GLUE methodology, Journal of Hydrology, 249, 11–29, https://doi.org/10.1016/S0022-1694(01)00421-8, 2001.

845 Bond, T. C., Doherty, S. J., Fahey, D. W., Forster, P. M., Berntsen, T., DeAngelo, B. J., Flanner, M. G., Ghan, S., Kärcher, B., Koch, D., Kinne, S., Kondo, Y., Quinn, P. K., Sarofim, M. C., Schultz, M. G., Schulz, M., Venkataraman, C., Zhang, H., Zhang, S., Bellouin, N., Guttikunda, S. K., Hopke, P. K., Jacobson, M. Z., Kaiser, J. W., Klimont, Z., Lohmann, U., Schwarz, J. P., Shindell, D., Storelvmo, T., Warren, S. G., and Zender, C. S.: Bounding the role of black carbon in the climate system: A scientific assessment, JGR Atmospheres, 118, 5380–5552, https://doi.org/10.1002/jgrd.50171, 2013.

850 Brock, C. A., Froyd, K. D., Dollner, M., Williamson, C. J., Schill, G. P., Murphy, D. M., Wagner, N. L., Kupc, A., Jimenez, J. L., Campuzano-Jost, P., Nault, B. A., Schroder, J. C., Day, D. A., Price, D. J., Weinzierl, B. B., Schwarz, J. P., Katich, J. M., Wang, S., Zeng, L. H., Webb, R., Dibb, J. E., Scheuer, E., Diskin, G. S., DiGangi, J. P., Bui, T. P., Dean-Day, J. M., Thompson, C. R., Peischl, J., Ryerson, T. B., Bourgeois, I., Daube, B. C., Commane, R., and Wofsy, S. C.: Atmospheric Tomography Mission (ATom)ATom: Comprehensive Aerosol Properties, 2016-2018, Version 2, https://doi.org/10.3334/ORNLDAAC/2111, 22 September 2022.

855 Browse, J., Carslaw, K. S., Arnold, S. R., Pringle, K., and Boucher, O.: The scavenging processes controlling the seasonal cycle in Arctic sulphate and black carbon aerosol, Atmos. Chem. Phys., 12, 6775–6798, https://doi.org/10.5194/acp-12-6775-2012, 2012.

Budhavant, K., Manoj, M. R., Nair, H. R. C. R., Gaita, S. M., Holmstrand, H., Salam, A., Muslim, A., Satheesh, S. K., and Gustafsson, Ö.: Changing optical properties of black carbon and brown carbon aerosols during long-range transport from the 860 Indo-Gangetic Plain to the equatorial Indian Ocean, Atmos. Chem. Phys., 24, 11911–11925, https://doi.org/10.5194/acp-24-11911-2024, 2024.

Cao, Y., Zhu, Y., Wang, M., Rosenfeld, D., Liang, Y., Liu, J., Liu, Z., and Bai, H.: Emission Reductions Significantly Reduce the Hemispheric Contrast in Cloud Droplet Number Concentration in Recent Two Decades, JGR Atmospheres, 128, e2022JD037417, https://doi.org/10.1029/2022JD037417, 2023.

865 Carslaw, K. S., Lee, L. A., Reddington, C. L., Pringle, K. J., Rap, A., Forster, P. M., Mann, G. W., Spracklen, D. V., Woodhouse, M. T., Regayre, L. A., and Pierce, J. R.: Large contribution of natural aerosols to uncertainty in indirect forcing, Nature, 503, 67–71, https://doi.org/10.1038/nature12674, 2013.

Chemke, R. and Dagan, G.: The Effects of the Spatial Distribution of Direct Anthropogenic Aerosols Radiative Forcing on Atmospheric Circulation, J. Climate, 31, 7129–7145, https://doi.org/10.1175/JCLI-D-17-0694.1, 2018.

870 Chen, D., Rojas, M., Samset, B. H., Cobb, K., Diongue Niang, A., Edwards, P., Emori, S., Faria, S. H., Hawkins, E., Hope, P., Huybrechts, P., Meinshausen, M., Mustafa, S. K., Plattner, G.-K., and Treguier, A.-M.: Framing, Context, and Methods, in: Climate Change 2021: The Physical Science Basis. Contribution of Working Group I to the Sixth Assessment Report of the Intergovernmental Panel on Climate Change, Cambridge University Press, Cambridge, United Kingdom and New York, 147–286, 2021.

875 Craig, P. S., Goldstein, M., Seheult, A. H., and Smith, J. A.: Pressure Matching for Hydrocarbon Reservoirs: A Case Study in the Use of Bayes Linear Strategies for Large Computer Experiments, in: Case Studies in Bayesian Statistics, vol. 121, edited by: Gatsonis, C., Hodges, J. S., Kass, R. E., McCulloch, R., Rossi, P., and Singpurwalla, N. D., Springer New York, New York, NY, 37–93, https://doi.org/10.1007/978-1-4612-2290-3_2, 1997.

880 Eidhammer, T., Gettelman, A., Thayer-Calder, K., Watson-Parris, D., Elsaesser, G., Morrison, H., Van Lier-Walqui, M., Song, C., and McCoy, D.: An extensible perturbed parameter ensemble for the Community Atmosphere Model version 6, Geosci. Model Dev., 17, 7835–7853, https://doi.org/10.5194/gmd-17-7835-2024, 2024.

Elsaesser, G. S., Van Lier-Walqui, M., Yang, Q., Kelley, M., Ackerman, A. S., Fridlind, A. M., Cesana, G. V., Schmidt, G. A., Wu, J., Behrangi, A., Camargo, S. J., De, B., Inoue, K., Leitmann-Niimi, N. M., and Strong, J. D. O.: Using Machine Learning to Generate a GISS ModelE Calibrated Physics Ensemble (CPE), J Adv Model Earth Syst, 17, e2024MS004713, 885 https://doi.org/10.1029/2024MS004713, 2025.

Endo, T., Yagoh, H., Sato, K., Matsuda, K., Hayashi, K., Noguchi, I., and Sawada, K.: Regional characteristics of dry deposition of sulfur and nitrogen compounds at EANET sites in Japan from 2003 to 2008, Atmospheric Environment, 45, 1259–1267, https://doi.org/10.1016/j.atmosenv.2010.12.003, 2011.

Eyring, V., Bony, S., Meehl, G. A., Senior, C. A., Stevens, B., Stouffer, R. J., and Taylor, K. E.: Overview of the Coupled 890 Model Intercomparison Project Phase 6 (CMIP6) experimental design and organization, Geosci. Model Dev., 9, 1937–1958, https://doi.org/10.5194/gmd-9-1937-2016, 2016.

Fierce, L., Bond, T. C., Bauer, S. E., Mena, F., and Riemer, N.: Black carbon absorption at the global scale is affected by particle-scale diversity in composition, Nat Commun, 7, 12361, https://doi.org/10.1038/ncomms12361, 2016.

Fierce, L., Yao, Y., Easter, R., Ma, P.-L., Sun, J., Wan, H., and Zhang, K.: Quantifying structural errors in cloud condensation 895 nuclei activity from reduced representation of aerosol size distributions, Journal of Aerosol Science, 181, 106388, https://doi.org/10.1016/j.jaerosci.2024.106388, 2024.

Forster, P., Storelvmo, T., Armour, K., Collins, W., Dufresne, J., Frame, D., Lunt, D., Mauritsen, T., Palmer, M., Watanabe, M., Wild, M., and Zhang, H.: The Earth's energy budget, climate feedbacks, and climate sensitivity, in: Climate Change 2021: The Physical Science Basis. Contribution of Working Group I to the Sixth Assessment Report of the Intergovernmental Panel 900 on Climate Change, V. Masson-Delmotte, P. Zhai, A. Pirani, S. L. Connors, C. Pean, S. Berger, N. Caud, Y. Chen, L. Goldfarb, M. I. Gomis, M. Huang, K. Leitzell, E. Lonnoy, J. B. R. Matthews, T. K. Maycock, T. Aterfield, O. Yelekci, R. Yu and B. Zhou, Cambridge University Press, 2021.

Gallo, F., Sanchez, K. J., Anderson, B. E., Bennett, R., Brown, M. D., Crosbie, E. C., Hostetler, C., Jordan, C., Yang Martin, M., Robinson, C. E., Russell, L. M., Shingler, T. J., Shook, M. A., Thornhill, K. L., Wiggins, E. B., Winstead, E. L., Wisthaler, 905 A., Ziemba, L. D., and Moore, R. H.: Measurement report: Aerosol vertical profiles over the western North Atlantic Ocean during the North Atlantic Aerosols and Marine Ecosystems Study (NAAMES), Atmos. Chem. Phys., 23, 1465–1490, https://doi.org/10.5194/acp-23-1465-2023, 2023.

Gettelman, A., Eidhammer, T., Duffy, M. L., McCoy, D. T., Song, C., and Watson-Parris, D.: The Interaction Between Climate Forcing and Feedbacks, JGR Atmospheres, 129, e2024JD040857, https://doi.org/10.1029/2024JD040857, 2024.

910 Ghan, S., Wang, M., Zhang, S., Ferrachat, S., Gettelman, A., Griesfeller, J., Kipling, Z., Lohmann, U., Morrison, H., Neubauer, D., Partridge, D. G., Stier, P., Takemura, T., Wang, H., and Zhang, K.: Challenges in constraining anthropogenic aerosol effects on cloud radiative forcing using present-day spatiotemporal variability, Proc Natl Acad Sci USA, 113, 5804–5811, https://doi.org/10.1073/pnas.1514036113, 2016.

Gosling, J. P.: SHELF: The Sheffield Elicitation Framework, in: Elicitation, vol. 261, edited by: Dias, L. C., Morton, A., and 915 Quigley, J., Springer International Publishing, Cham, 61–93, https://doi.org/10.1007/978-3-319-65052-4_4, 2018.

Grosvenor, D. P. and Carslaw, K. S.: The decomposition of cloud–aerosol forcing in the UK Earth System Model (UKESM1), Atmos. Chem. Phys., 20, 15681–15724, https://doi.org/10.5194/acp-20-15681-2020, 2020.

Gryspeerdt, E., Quaas, J., and Bellouin, N.: Constraining the aerosol influence on cloud fraction: AEROSOLS AND CLOUD FRACTION, J. Geophys. Res. Atmos., 121, 3566–3583, https://doi.org/10.1002/2015JD023744, 2016.

920 Halmer, M. M., Schmincke, H.-U., and Graf, H.-F.: The annual volcanic gas input into the atmosphere, in particular into the stratosphere: a global data set for the past 100 years, Journal of Volcanology and Geothermal Research, 115, 511–528, https://doi.org/10.1016/S0377-0273(01)00318-3, 2002.

Hamilton, D. S., Lee, L. A., Pringle, K. J., Reddington, C. L., Spracklen, D. V., and Carslaw, K. S.: Occurrence of pristine aerosol environments on a polluted planet, Proc Natl Acad Sci USA, 111, 18466–18471, 925 https://doi.org/10.1073/pnas.1415440111, 2014.

Hoffmann, J., Bauer, P., Sandu, I., Wedi, N., Geenen, T., and Thiemert, D.: Destination Earth – A digital twin in support of climate services, Climate Services, 30, 100394, https://doi.org/10.1016/j.cliser.2023.100394, 2023.

Hourdin, F., Mauritsen, T., Gettelman, A., Golaz, J.-C., Balaji, V., Duan, Q., Folini, D., Ji, D., Klocke, D., Qian, Y., Rauser, F., Rio, C., Tomassini, L., Watanabe, M., and Williamson, D.: The Art and Science of Climate Model Tuning, Bulletin of the 930 American Meteorological Society, 98, 589–602, https://doi.org/10.1175/BAMS-D-15-00135.1, 2017.

Huebert, B. J., Bates, T., Russell, P. B., Shi, G., Kim, Y. J., Kawamura, K., Carmichael, G., and Nakajima, T.: An overview of ACE-Asia: Strategies for quantifying the relationships between Asian aerosols and their climatic impacts, J. Geophys. Res., 108, 2003JD003550, https://doi.org/10.1029/2003JD003550, 2003.

Intergovernmental Panel On Climate Change (Ipcc): Climate Change 2021 – The Physical Science Basis: Working Group I 935 Contribution to the Sixth Assessment Report of the Intergovernmental Panel on Climate Change, 1st ed., Cambridge University Press, https://doi.org/10.1017/9781009157896, 2023.

Jia, H. and Quaas, J.: Nonlinearity of the cloud response postpones climate penalty of mitigating air pollution in polluted regions, Nat. Clim. Chang., 13, 943–950, https://doi.org/10.1038/s41558-023-01775-5, 2023.

Johnson, J. S., Regayre, L. A., Yoshioka, M., Pringle, K. J., Turnock, S. T., Browse, J., Sexton, D. M. H., Rostron, J. W., 940 Schutgens, N. A. J., Partridge, D. G., Liu, D., Allan, J. D., Coe, H., Ding, A., Cohen, D. D., Atanacio, A., Vakkari, V., Asmi, E., and Carslaw, K. S.: Robust observational constraint of uncertain aerosol processes and emissions in a climate model and the effect on aerosol radiative forcing, Atmos. Chem. Phys., 20, 9491–9524, https://doi.org/10.5194/acp-20-9491-2020, 2020.

Kahn, R. A., Andrews, E., Brock, C. A., Chin, M., Feingold, G., Gettelman, A., Levy, R. C., Murphy, D. M., Nenes, A., Pierce, J. R., Popp, T., Redemann, J., Sayer, A. M., Da Silva, A. M., Sogacheva, L., and Stier, P.: Reducing Aerosol Forcing 945 Uncertainty by Combining Models With Satellite and Within-The-Atmosphere Observations: A Three-Way Street, Reviews of Geophysics, 61, e2022RG000796, https://doi.org/10.1029/2022RG000796, 2023.

Knutti, R., Masson, D., and Gettelman, A.: Climate model genealogy: Generation CMIP5 and how we got there: CLIMATE MODEL GENEALOGY, Geophys. Res. Lett., 40, 1194–1199, https://doi.org/10.1002/grl.50256, 2013.

Kokkola, H., Tonttila, J., Calderón, S. M., Romakkaniemi, S., Lipponen, A., Peräkorpi, A., Mielonen, T., Gryspeerdt, E., 950 Virtanen, T. H., Kolmonen, P., and Arola, A.: Model analysis of biases in the satellite-diagnosed aerosol effect on the cloud liquid water path, Atmos. Chem. Phys., 25, 1533–1543, https://doi.org/10.5194/acp-25-1533-2025, 2025.

Kuma, P., Bender, F. A. -M., and Jönsson, A. R.: Climate Model Code Genealogy and Its Relation to Climate Feedbacks and Sensitivity, J Adv Model Earth Syst, 15, e2022MS003588, https://doi.org/10.1029/2022MS003588, 2023.

955 Lack, D. A. and Cappa, C. D.: Impact of brown and clear carbon on light absorption enhancement, single scatter albedo and absorption wavelength dependence of black carbon, Atmos. Chem. Phys., 10, 4207–4220, https://doi.org/10.5194/acp-10-4207-2010, 2010.

Lee, L. A., Carslaw, K. S., Pringle, K. J., and Mann, G. W.: Mapping the uncertainty in global CCN using emulation, Atmos. Chem. Phys., 12, 9739–9751, https://doi.org/10.5194/acp-12-9739-2012, 2012.

Lee, L. A., Reddington, C. L., and Carslaw, K. S.: On the relationship between aerosol model uncertainty and radiative forcing uncertainty, Proc Natl Acad Sci USA, 113, 5820–5827, https://doi.org/10.1073/pnas.1507050113, 2016.

960 Liu, Z., Bollasina, M. A., and Wilcox, L. J.: Impact of Asian aerosols on the summer monsoon strongly modulated by regional precipitation biases, Atmos. Chem. Phys., 24, 7227–7252, https://doi.org/10.5194/acp-24-7227-2024, 2024.

Loeb, N. G., Doelling, D. R., Wang, H., Su, W., Nguyen, C., Corbett, J. G., Liang, L., Mitrescu, C., Rose, F. G., and Kato, S.: Clouds and the Earth's Radiant Energy System (CERES) Energy Balanced and Filled (EBAF) Top-of-Atmosphere (TOA) Edition-4.0 Data Product, J. Climate, 31, 895–918, https://doi.org/10.1175/JCLI-D-17-0208.1, 2018.

965 Mather, J. H. and Voyles, J. W.: The Arm Climate Research Facility: A Review of Structure and Capabilities, Bull. Amer. Meteor. Soc., 94, 377–392, https://doi.org/10.1175/BAMS-D-11-00218.1, 2013.

McCoy, I. L., McCoy, D. T., Wood, R., Regayre, L., Watson-Parris, D., Grosvenor, D. P., Mulcahy, J. P., Hu, Y., Bender, F. A.-M., Field, P. R., Carslaw, K. S., and Gordon, H.: The hemispheric contrast in cloud microphysical properties constrains aerosol forcing, Proceedings of the National Academy of Sciences, 117, 189980–19006, https://doi.org/10.1073/pnas.1922502117, 2020.

McNeall, D., Williams, J., Booth, B., Betts, R., Challenor, P., Wiltshire, A., and Sexton, D.: The impact of structural error on parameter constraint in a climate model, Earth Syst. Dynam., 7, 917–935, https://doi.org/10.5194/esd-7-917-2016, 2016.

Metzger, A., Verheggen, B., Dommen, J., Duplissy, J., Prevot, A. S. H., Weingartner, E., Riipinen, I., Kulmala, M., Spracklen, D. V., Carslaw, K. S., and Baltensperger, U.: Evidence for the role of organics in aerosol particle formation under atmospheric conditions, Proc. Natl. Acad. Sci. U.S.A., 107, 6646–6651, https://doi.org/10.1073/pnas.0911330107, 2010.

Mikkelsen, A., McCoy, D. T., Eidhammer, T., Gettelman, A., Song, C., Gordon, H., and McCoy, I. L.: Constraining Aerosol-Cloud Adjustments by Uniting Surface Observations with a Perturbed Parameter Ensemble, https://doi.org/10.5194/egusphere-2024-2158, 30 August 2024.

980 Mulcahy, J. P., Johnson, C., Jones, C. G., Povey, A. C., Scott, C. E., Sellar, A., Turnock, S. T., Woodhouse, M. T., Abraham, N. L., Andrews, M. B., Bellouin, N., Browse, J., Carslaw, K. S., Dalvi, M., Folberth, G. A., Glover, M., Grosvenor, D. P., Hardacre, C., Hill, R., Johnson, B., Jones, A., Kipling, Z., Mann, G., Mollard, J., O'Connor, F. M., Palmiéri, J., Reddington, C., Rumbold, S. T., Richardson, M., Schutgens, N. A. J., Stier, P., Stringer, M., Tang, Y., Walton, J., Woodward, S., and Yool, A.: Description and evaluation of aerosol in UKESM1 and HadGEM3-GC3.1 CMIP6 historical simulations, Geosci. Model Dev., 13, 6383–6423, https://doi.org/10.5194/gmd-13-6383-2020, 2020.

Mülmenstädt, J. and Wilcox, L. J.: The Fall and Rise of the Global Climate Model, J Adv Model Earth Syst, 13, e2021MS002781, https://doi.org/10.1029/2021MS002781, 2021.

Mülmenstädt, J., Ackerman, A. S., Fridlind, A. M., Huang, M., Ma, P.-L., Mahfouz, N., Bauer, S. E., Burrows, S. M., Christensen, M. W., Dipu, S., Gettelman, A., Leung, L. R., Tornow, F., Quaas, J., Varble, A. C., Wang, H., Zhang, K., and Zheng, Y.: Can general circulation models (GCMs) represent cloud liquid water path adjustments to aerosol–cloud interactions?, Atmos. Chem. Phys., 24, 13633–13652, https://doi.org/10.5194/acp-24-13633-2024, 2024.

Murphy, D. M., Froyd, K. D., Bian, H., Brock, C. A., Dibb, J. E., DiGangi, J. P., Diskin, G., Dollner, M., Kupc, A., Scheuer, E. M., Schill, G. P., Weinzierl, B., Williamson, C. J., and Yu, P.: The distribution of sea-salt aerosol in the global troposphere, Atmos. Chem. Phys., 19, 4093–4104, https://doi.org/10.5194/acp-19-4093-2019, 2019.

O'Hagan, A.: Bayesian analysis of computer code outputs: A tutorial, Reliability Engineering & System Safety, 91, 1290–1300, https://doi.org/10.1016/j.ress.2005.11.025, 2006.

Peace, A. H., Carslaw, K. S., Lee, L. A., Regayre, L. A., Booth, B. B. B., Johnson, J. S., and Bernie, D.: Effect of aerosol radiative forcing uncertainty on projected exceedance year of a 1.5 °C global temperature rise, Environ. Res. Lett., 15, 0940a6, https://doi.org/10.1088/1748-9326/aba20c, 2020.

Peace, A. H., Booth, B. B. B., Regayre, L. A., Carslaw, K. S., Sexton, D. M. H., Bonfils, C. J. W., and Rostron, J. W.: Evaluating Uncertainty in Aerosol Forcing of Tropical Precipitation Shifts, Earth system change: climate prediction, https://doi.org/10.5194/esd-2022-11, 2022.

Pedregosa, F., Varoquaux, G., Gramfort, A., Michel, V., Thirion, B., Grisel, O., Blondel, M., Prettenhofer, P., Weiss, R., Dubourg, V., Vanderplas, J., Passos, A., and Cournapeau, D.: Scikit-learn: Machine Learning in Python, J. Mach. Learn. Res., 12, 2825–2830, 2011.

Petrenko, M., Kahn, R., Chin, M., Bauer, S. E., Bergman, T., Bian, H., Curci, G., Johnson, B., Kaiser, J. W., Kipling, Z., Kokkola, H., Liu, X., Mezuman, K., Mielonen, T., Myhre, G., Pan, X., Protonotariou, A., Remy, S., Skeie, R. B., Stier, P., Takemura, T., Tsigaridis, K., Wang, H., Watson-Parris, D., and Zhang, K.: Biomass burning emission analysis based on MODIS aerosol optical depth and AeroCom multi-model simulations: implications for model constraints and emission inventories, Atmos. Chem. Phys., 25, 1545–1567, https://doi.org/10.5194/acp-25-1545-2025, 2025.

Price, R., Orr, A., Field, P. F., Mace, G., and Protat, A.: Simulation of Cloud Processes Over Offshore Coastal Antarctica Using the High-Resolution Regional UK Met Office Unified Model With Interactive Aerosols, JGR Atmospheres, 130, e2024JD042109, https://doi.org/10.1029/2024JD042109, 2025.

Proske, U., Ferrachat, S., Neubauer, D., Staab, M., and Lohmann, U.: Assessing the potential for simplification in global climate model cloud microphysics, Atmos. Chem. Phys., 22, 4737–4762, https://doi.org/10.5194/acp-22-4737-2022, 2022.

Qian, Y., Wan, H., Yang, B., Golaz, J., Harrop, B., Hou, Z., Larson, V. E., Leung, L. R., Lin, G., Lin, W., Ma, P., Ma, H., Rasch, P., Singh, B., Wang, H., Xie, S., and Zhang, K.: Parametric Sensitivity and Uncertainty Quantification in the Version 1 of E3SM Atmosphere Model Based on Short Perturbed Parameter Ensemble Simulations, J. Geophys. Res. Atmos., 123, https://doi.org/10.1029/2018JD028927, 2018.

Quaas, J., Arola, A., Cairns, B., Christensen, M., Deneke, H., Ekman, A. M. L., Feingold, G., Fridlind, A., Gryspeerdt, E., Hasekamp, O., Li, Z., Lipponen, A., Ma, P.-L., Mülmenstädt, J., Nenes, A., Penner, J. E., Rosenfeld, D., Schrödner, R., Sinclair, K., Sourdeval, O., Stier, P., Tesche, M., Van Diedenhoven, B., and Wendisch, M.: Constraining the Twomey effect from satellite observations: issues and perspectives, Atmos. Chem. Phys., 20, 15079–15099, https://doi.org/10.5194/acp-20-15079-2020, 2020.

Regayre, L.: Figure creation code and dependencies for Reamining aerosol forcing uncertainty after observational constraint and the processes that cause it, Regayre et al., (2025) submitted to ACPD, https://doi.org/10.5281/ZENODO.16686812, 2025.

Regayre, L. A., Pringle, K. J., Lee, L. A., Rap, A., Browse, J., Mann, G. W., Reddington, C. L., Carslaw, K. S., Booth, B. B. B., and Woodhouse, M. T.: The Climatic Importance of Uncertainties in Regional Aerosol–Cloud Radiative Forcings over Recent Decades, Journal of Climate, 28, 6589–6607, https://doi.org/10.1175/JCLI-D-15-0127.1, 2015.

1030 Regayre, L. A., Johnson, J. S., Yoshioka, M., Pringle, K. J., Sexton, D. M. H., Booth, B. B. B., Lee, L. A., Bellouin, N., and Carslaw, K. S.: Aerosol and physical atmosphere model parameters are both important sources of uncertainty in aerosol ERF, Atmos. Chem. Phys., 18, 9975–10006, https://doi.org/10.5194/acp-18-9975-2018, 2018.

Regayre, L. A., Schmale, J., Johnson, J. S., Tatzelt, C., Baccarini, A., Henning, S., Yoshioka, M., Stratmann, F., Gysel-Beer, M., Grosvenor, D. P., and Carslaw, K. S.: The value of remote marine aerosol measurements for constraining radiative forcing
1035 uncertainty, Atmos. Chem. Phys., 20, 10063–10072, https://doi.org/10.5194/acp-20-10063-2020, 2020.

Regayre, L. A., Deaconu, L., Grosvenor, D. P., Sexton, D. M. H., Symonds, C., Langton, T., Watson-Paris, D., Mulcahy, J. P., Pringle, K. J., Richardson, M., Johnson, J. S., Rostron, J. W., Gordon, H., Lister, G., Stier, P., and Carslaw, K. S.: Identifying climate model structural inconsistencies allows for tight constraint of aerosol radiative forcing, Atmos. Chem. Phys., 23, 8749–8768, https://doi.org/10.5194/acp-23-8749-2023, 2023.

1040 Regayre, L. A., Carslaw, K. S., Deaconu, L., Symonds, C., Richardson, M., Langton, T., Watson-Parris, D., and Stier, P.: A-CURE: Monthly mean perturbed parameter ensemble data, https://catalogue.ceda.ac.uk/uuid/b735718d66c1403fbf6b93ba3bd3b1a9.

Regayre, L. eighton A., Pringle, K. J., Booth, B. B. B., Lee, L. A., Mann, G. W., Browse, J., Woodhouse, M. T., Rap, A., Reddington, C. L., and Carslaw, K. S.: Uncertainty in the magnitude of aerosol-cloud radiative forcing over recent decades,
1045 Geophys. Res. Lett., 41, 9040–9049, https://doi.org/10.1002/2014GL062029, 2014.

Reutter, P., Su, H., Trentmann, J., Simmel, M., Rose, D., Gunthe, S. S., Wernli, H., Andreae, M. O., and Pöschl, U.: Aerosol-and updraft-limited regimes of cloud droplet formation: influence of particle number, size and hygroscopicity on the activation of cloud condensation nuclei (CCN), Atmos. Chem. Phys., 9, 7067–7080, https://doi.org/10.5194/acp-9-7067-2009, 2009.

Rostron, J. W., Sexton, D. M. H., McSweeney, C. F., Yamazaki, K., Andrews, T., Furtado, K., Ringer, M. A., and Tsushima,
1050 Y.: The impact of performance filtering on climate feedbacks in a perturbed parameter ensemble, Clim Dyn, 55, 521–551, https://doi.org/10.1007/s00382-020-05281-8, 2020.

Rostron, J. W., Sexton, D. M. H., Furtado, K., and Tsushima, Y.: A clearer view of systematic errors in model development: two practical approaches using perturbed parameter ensembles., https://doi.org/10.21203/rs.3.rs-5025285/v1, 19 March 2025.

Saltelli, A., Aleksankina, K., Becker, W., Fennell, P., Ferretti, F., Holst, N., Li, S., and Wu, Q.: Why so many published
1055 sensitivity analyses are false: A systematic review of sensitivity analysis practices, Environmental Modelling & Software, 114, 29–39, https://doi.org/10.1016/j.envsoft.2019.01.012, 2019.

Salter, J. M., Williamson, D. B., Scinocca, J., and Kharin, V.: Uncertainty Quantification for Computer Models With Spatial Output Using Calibration-Optimal Bases, Journal of the American Statistical Association, 114, 1800–1814, https://doi.org/10.1080/01621459.2018.1514306, 2019.

1060 Sand, M., Samset, B. H., Myhre, G., Gliß, J., Bauer, S. E., Bian, H., Chin, M., Checa-Garcia, R., Ginoux, P., Kipling, Z., Kirkevåg, A., Kokkola, H., Le Sager, P., Lund, M. T., Matsui, H., Van Noije, T., Olivié, D. J. L., Remy, S., Schulz, M., Stier, P., Stjern, C. W., Takemura, T., Tsigaridis, K., Tsyro, S. G., and Watson-Parris, D.: Aerosol absorption in global models from AeroCom phase III, Atmos. Chem. Phys., 21, 15929–15947, https://doi.org/10.5194/acp-21-15929-2021, 2021.

Sanderson, B. M., Knutti, R., and Caldwell, P.: A Representative Democracy to Reduce Interdependency in a Multimodel
1065 Ensemble, Journal of Climate, 28, 5171–5194, https://doi.org/10.1175/JCLI-D-14-00362.1, 2015.

Sansom, R. W. N., Carslaw, K. S., Johnson, J. S., and Lee, L.: An Emulator of Stratocumulus Cloud Response to Two Cloud-Controlling Factors Accounting for Internal Variability, J Adv Model Earth Syst, 16, e2023MS004179, https://doi.org/10.1029/2023MS004179, 2024.

1070 Schmale, J., Baccarini, A., Thurnherr, I., Henning, S., Efraim, A., Regayre, L., Bolas, C., Hartmann, M., Welti, A., Lehtipalo, K., Aemisegger, F., Tatzelt, C., Landwehr, S., Modini, R. L., Tummon, F., Johnson, J. S., Harris, N., Schnaiter, M., Toffoli, A., Derkani, M., Bukowiecki, N., Stratmann, F., Dommen, J., Baltensperger, U., Wernli, H., Rosenfeld, D., Gysel-Beer, M., and Carslaw, K. S.: Overview of the Antarctic Circumnavigation Expedition: Study of Preindustrial-like Aerosols and Their Climate Effects (ACE-SPACE), Bulletin of the American Meteorological Society, 100, 2260–2283, https://doi.org/10.1175/BAMS-D-18-0187.1, 2019.

1075 Schutgens, N., Tsyro, S., Gryspeerdt, E., Goto, D., Weigum, N., Schulz, M., and Stier, P.: On the spatio-temporal representativeness of observations, Atmos. Chem. Phys., 17, 9761–9780, https://doi.org/10.5194/acp-17-9761-2017, 2017.

Sellar, A. A., Jones, C. G., Mulcahy, J. P., Tang, Y., Yool, A., Wiltshire, A., O'Connor, F. M., Stringer, M., Hill, R., Palmieri, J., Woodward, S., Mora, L., Kuhlbrodt, T., Rumbold, S. T., Kelley, D. I., Ellis, R., Johnson, C. E., Walton, J., Abraham, N. L., Andrews, M. B., Andrews, T., Archibald, A. T., Berthou, S., Burke, E., Blockley, E., Carslaw, K., Dalvi, M., Edwards, J., 1080 Folberth, G. A., Gedney, N., Griffiths, P. T., Harper, A. B., Hendry, M. A., Hewitt, A. J., Johnson, B., Jones, A., Jones, C. D., Keeble, J., Liddicoat, S., Morgenstern, O., Parker, R. J., Predoi, V., Robertson, E., Siahaan, A., Smith, R. S., Swaminathan, R., Woodhouse, M. T., Zeng, G., and Zerroukat, M.: UKESM1: Description and Evaluation of the U.K. Earth System Model, J. Adv. Model. Earth Syst., 11, 4513–4558, https://doi.org/10.1029/2019MS001739, 2019.

Servén, D., Brummitt, C., Abedi, H., and Hlink: dswah/pyGAM: v0.8.0, , https://doi.org/10.5281/ZENODO.1208723, 2018.

1085 Sexton, D. M. H., Murphy, J. M., Collins, M., and Webb, M. J.: Multivariate probabilistic projections using imperfect climate models part I: outline of methodology, Clim Dyn, 38, 2513–2542, https://doi.org/10.1007/s00382-011-1208-9, 2012.

Sexton, D. M. H., McSweeney, C. F., Rostron, J. W., Yamazaki, K., Booth, B. B. B., Murphy, J. M., Regayre, L., Johnson, J. S., and Karmalkar, A. V.: A perturbed parameter ensemble of HadGEM3-GC3.05 coupled model projections: part 1: selecting the parameter combinations, Clim Dyn, 56, 3395–3436, https://doi.org/10.1007/s00382-021-05709-9, 2021.

1090 Shindell, D. T.: Inhomogeneous forcing and transient climate sensitivity, Nature Clim Change, 4, 274–277, https://doi.org/10.1038/nclimate2136, 2014.

Sprintall, J., Coles, V. J., Reed, K. A., Butler, A. H., Foltz, G. R., Penny, S. G., and Seo, H.: Best Practice Strategies for Process Studies Designed to Improve Climate Modeling, Bulletin of the American Meteorological Society, 101, E1842–E1850, https://doi.org/10.1175/BAMS-D-19-0263.1, 2020.

1095 Strong, M., Oakley, J. E., and Brennan, A.: Estimating Multiparameter Partial Expected Value of Perfect Information from a Probabilistic Sensitivity Analysis Sample: A Nonparametric Regression Approach, Med Decis Making, 34, 311–326, https://doi.org/median

, 2014.

Sun, C., Zhang, Y., Liang, B., Gao, M., Sun, X., Li, F., Ni, X., Sun, Q., Ou, H., Chen, D., Zhou, S., and Zhao, J.: Morphological 1100 and optical properties of carbonaceous aerosol particles from ship emissions and biomass burning during a summer cruise measurement in the South China Sea, Atmos. Chem. Phys., 24, 3043–3063, https://doi.org/10.5194/acp-24-3043-2024, 2024.

Walters, D., Baran, A. J., Boutle, I., Brooks, M., Earnshaw, P., Edwards, J., Furtado, K., Hill, P., Lock, A., Manners, J., Morcrette, C., Mulcahy, J., Sanchez, C., Smith, C., Stratton, R., Tennant, W., Tomassini, L., Van Weverberg, K., Vosper, S.,

Willett, M., Browse, J., Bushell, A., Carslaw, K., Dalvi, M., Essery, R., Gedney, N., Hardiman, S., Johnson, B., Johnson, C.,
1105 Jones, A., Jones, C., Mann, G., Milton, S., Rumbold, H., Sellar, A., Ujiie, M., Whitall, M., Williams, K., and Zerroukat, M.:
The Met Office Unified Model Global Atmosphere 7.0/7.1 and JULES Global Land 7.0 configurations, Geosci. Model Dev.,
12, 1909–1963, https://doi.org/10.5194/gmd-12-1909-2019, 2019.

Wang, J., Wood, R., Jensen, M. P., Chiu, J. C., Liu, Y., Lamer, K., Desai, N., Giangrande, S. E., Knopf, D. A., Kollias, P.,
Laskin, A., Liu, X., Lu, C., Mechem, D., Mei, F., Starzec, M., Tomlinson, J., Wang, Y., Yum, S. S., Zheng, G., Aiken, A. C.,
1110 Azevedo, E. B., Blanchard, Y., China, S., Dong, X., Gallo, F., Gao, S., Ghate, V. P., Glienke, S., Goldberger, L., Hardin, J.
C., Kuang, C., Luke, E. P., Matthews, A. A., Miller, M. A., Moffet, R., Pekour, M., Schmid, B., Sedlacek, A. J., Shaw, R. A.,
Shilling, J. E., Sullivan, A., Suski, K., Veghte, D. P., Weber, R., Wyant, M., Yeom, J., Zawadowicz, M., and Zhang, Z.:
Aerosol and Cloud Experiments in the Eastern North Atlantic (ACE-ENA), Bulletin of the American Meteorological Society,
103, E619–E641, https://doi.org/10.1175/BAMS-D-19-0220.1, 2022.

1115 Watson-Parris, D. and Smith, C. J.: Large uncertainty in future warming due to aerosol forcing, Nat. Clim. Chang., 12, 1111–
1113, https://doi.org/10.1038/s41558-022-01516-0, 2022.

Williams, A. I. L., Stier, P., Dagan, G., and Watson-Parris, D.: Strong control of effective radiative forcing by the spatial
pattern of absorbing aerosol, Nat. Clim. Chang., 12, 735–742, https://doi.org/10.1038/s41558-022-01415-4, 2022.

Williams, K. D., Copsey, D., Blockley, E. W., Bodas-Salcedo, A., Calvert, D., Comer, R., Davis, P., Graham, T., Hewitt, H.
1120 T., Hill, R., Hyder, P., Ineson, S., Johns, T. C., Keen, A. B., Lee, R. W., Megann, A., Milton, S. F., Rae, J. G. L., Roberts, M.
J., Scaife, A. A., Schiemann, R., Storkey, D., Thorpe, L., Watterson, I. G., Walters, D. N., West, A., Wood, R. A., Woollings,
T., and Xavier, P. K.: The Met Office Global Coupled Model 3.0 and 3.1 (GC3.0 and GC3.1) Configurations, J. Adv. Model.
Earth Syst., 10, 357–380, https://doi.org/10.1002/2017MS001115, 2018.

Williamson, D., Goldstein, M., Allison, L., Blaker, A., Challenor, P., Jackson, L., and Yamazaki, K.: History matching for
1125 exploring and reducing climate model parameter space using observations and a large perturbed physics ensemble, Clim Dyn,
41, 1703–1729, https://doi.org/10.1007/s00382-013-1896-4, 2013.

Wood, R., Mechoso, C. R., Bretherton, C. S., Weller, R. A., Huebert, B., Straneo, F., Albrecht, B. A., Coe, H., Allen, G.,
Vaughan, G., Daum, P., Fairall, C., Chand, D., Gallardo Klenner, L., Garreaud, R., Grados, C., Covert, D. S., Bates, T. S.,
Krejci, R., Russell, L. M., De Szoeke, S., Brewer, A., Yuter, S. E., Springston, S. R., Chaigneau, A., Toniazzo, T., Minnis, P.,
1130 Palikonda, R., Abel, S. J., Brown, W. O. J., Williams, S., Fochesatto, J., Brioude, J., and Bower, K. N.: The VAMOS Ocean-
Cloud-Atmosphere-Land Study Regional Experiment (VOCALS-REx): goals, platforms, and field operations, Atmos. Chem.
Phys., 11, 627–654, https://doi.org/10.5194/acp-11-627-2011, 2011.

Yeom, J. M., Yum, S. S., Shaw, R. A., La, I., Wang, J., Lu, C., Liu, Y., Mei, F., Schmid, B., and Matthews, A.: Vertical
Variations of Cloud Microphysical Relationships in Marine Stratocumulus Clouds Observed During the ACE-ENA Campaign,
1135 JGR Atmospheres, 126, e2021JD034700, https://doi.org/10.1029/2021JD034700, 2021.

Yoshioka, M., Regayre, L. A., Pringle, K. J., Johnson, J. S., Mann, G. W., Partridge, D. G., Sexton, D. M. H., Lister, G. M. S.,
Schutgens, N., Stier, P., Kipling, Z., Bellouin, N., Browse, J., Booth, B. B. B., Johnson, C. E., Johnson, B., Mollard, J. D. P.,
Lee, L., and Carslaw, K. S.: Ensembles of Global Climate Model Variants Designed for the Quantification and Constraint of
Uncertainty in Aerosols and Their Radiative Forcing, J. Adv. Model. Earth Syst., 11, 3728–3754,
1140 https://doi.org/10.1029/2019MS001628, 2019.

Zheng, G., Wang, Y., Aiken, A. C., Gallo, F., Jensen, M. P., Kollias, P., Kuang, C., Luke, E., Springston, S., Uin, J., Wood,
R., and Wang, J.: Marine boundary layer aerosol in the eastern North Atlantic: seasonal variations and key controlling
processes, Atmos. Chem. Phys., 18, 17615–17635, https://doi.org/10.5194/acp-18-17615-2018, 2018.

Zhong, Q., Schutgens, N., Van Der Werf, G. R., Takemura, T., Van Noije, T., Mielonen, T., Checa-Garcia, R., Lohmann, U., Kirkevåg, A., Olivié, D. J. L., Kokkola, H., Matsui, H., Kipling, Z., Ginoux, P., Le Sager, P., Rémy, S., Bian, H., Chin, M., Zhang, K., Bauer, S. E., and Tsigaridis, K.: Threefold reduction of modeled uncertainty in direct radiative effects over biomass burning regions by constraining absorbing aerosols, Sci. Adv., 9, eadi3568, https://doi.org/10.1126/sciadv.adi3568, 2023.

Zhuang, B. L., Liu, L., Shen, F. H., Wang, T. J., and Han, Y.: Semidirect radiative forcing of internal mixed black carbon cloud droplet and its regional climatic effect over China, J. Geophys. Res., 115, 2009JD013165, https://doi.org/10.1029/2009JD013165, 2010.